


Feedback and dynamical masses in high- z galaxies: the advent of high-resolution NIRSpec spectroscopy

A. Saldana-Lopez,¹  J. Chisholm,² S. Gazagnes,² R. Endsley,² M. J. Hayes,¹
D. A. Berg,² S. L. Finkelstein,² S. R. Flury,³ N. G. Guseva,⁴ A. Henry,⁵ Y. I. Izotov,⁴
E. Lambrides,⁶ R. Marques-Chaves,⁷ C. T. Richardson,⁸

¹ Department of Astronomy, Oskar Klein Centre, Stockholm University, 106 91 Stockholm, Sweden

² Department of Astronomy, The University of Texas at Austin, 2515 Speedway, Stop C1400, Austin, TX 78712-1205, USA

³ Institute for Astronomy, University of Edinburgh, Royal Observatory, Edinburgh, EH9 3HJ, UK

⁴ Bogolyubov Institute for Theoretical Physics, National Academy of Sciences of Ukraine, 14-b Metrolohichna str., Kyiv, 03143, Ukraine

⁵ Space Telescope Science Institute, 3700 San Martin Drive Baltimore, MD 21218, USA

⁶ Astrophysics Science Division, Code 662, NASA Goddard Space Flight Center, 8800 Greenbelt Rd, Greenbelt, MD 20771, USA

⁷ Department of Astronomy, University of Geneva, 51 Chemin Pegasi, 1290 Versoix, Switzerland

⁸ Elon University, 100 Campus Drive, Elon, NC 27244

Accepted 2025 xxxx XX. Received 2025 xxxx XX; in original form 2025 January 28

ABSTRACT

Stellar feedback is an essential step in the baryon cycle of galaxies, but it remains unconstrained beyond Cosmic Noon. We study the ionized gas kinematics, dynamical mass and gas-flow properties of a sample of 16 sub- L^* star-forming galaxies at $4 \leq z \leq 7.6$, using high-resolution JWST/NIRSpec observations. The emission lines are resolved, with velocity dispersions (σ_{gas} (km s⁻¹) $\approx 38 - 96$) comparable to more massive galaxies at Cosmic Noon. From σ_{gas} and the galaxy size ($r_e = 400 - 960$ pc), we estimate the dynamical mass to be $\log M_{\text{dyn}}/M_{\odot} = 9.25 - 10.25$. Stellar-to-dynamical mass ratios are low ($\log M_{\star}/M_{\text{dyn}} \in [-0.5, -2]$) and decrease with increasing SFR surface density (Σ_{SFR}). We estimate the gas surface densities assuming a star-formation law, but the gas masses do not balance the baryon-to-dynamical mass ratios, which would require a decrease in the star-formation efficiency. We find evidence of ionized outflows in five out of the sixteen galaxies, based on the need of broad components to reproduce the emission-line wings. We only observe outflows from galaxies undergoing recent bursts of star formation $\text{SFR}_{10}/\text{SFR}_{100} \geq 1$, with elevated Σ_{SFR} and low M_{\star}/M_{dyn} . This links high gas surface densities to increased outflow incidence and lower M_{\star}/M_{dyn} . With moderate outflow velocities (v_{flow} (km s⁻¹) = 150 – 250) and mass outflow rates ($\dot{M}_{\text{flow}}/M_{\odot}\text{yr}^{-1} = 0.2 - 5$), these high-redshift galaxies appear more efficient at removing baryons than low-redshift galaxies with similar M_{\star} , showing mass loading-factors of $\dot{M}_{\text{flow}}/\text{SFR} = 0.04 - 0.4$. For their given dynamical mass, the outflow velocities exceed the escape velocities, meaning that they may eventually enrich the Circumgalactic Medium.

Key words: cosmology: dark ages, reionization, first stars – galaxies: evolution, high-redshift, ISM, star-formation – ISM: jets and outflows, kinematics and dynamics

1 INTRODUCTION

Gas in galaxies collapses under gravity in the depths of potential wells to forge stellar mass. However, galaxies are inefficient at converting gas into stars (e.g., see White & Frenk 1991; Vogelsberger et al. 2013; Wechsler & Tinker 2018). Abundance matching suggests that the stellar-to-halo mass ratio is below the constant $\approx 20\%$ of the cosmic baryon abundance predicted by the Λ CDM formalism, reaching its maximum at halo masses of $\log M_h/M_{\odot} \approx 12$, and declining on both sides of this mass (e.g., Conroy & Wechsler 2009; Behroozi et al. 2013). This decreased M_{\star}/M_h ratio can be explained if significant amounts of baryons are either prevented to form stars or removed from the star-forming regions, via the so-called *feedback* mechanisms (e.g., Hernquist & Springel 2003;

Hayward & Hopkins 2017), while non-baryons remain within the halos.

Different feedback modes will operate at the high or low mass ends of the halo mass function (e.g., Dekel & Silk 1986; Fabian 2012). In the high mass regime ($\log M_h/M_{\odot} > 12$), thermal feedback from active galactic nuclei (AGN) reduces the ability of the gas to cool to further accrete and form stars (e.g., Rees & Ostriker 1977). Together with the mechanical and radiative feedback in the form of jets and energetic outflows (e.g., Heckman & Best 2014), both processes may regulate the star formation in such high-mass systems (e.g., Villar-Martín et al. 2011; Leung et al. 2019; Revalski et al. 2021; Ruschel-Dutra et al. 2021; Flury et al. 2023), resulting in a co-evolution between the mass assembly of the host and the AGN activity (e.g., Harrison et al. 2014; Fiore et al. 2017).

In low-mass haloes, feedback from massive stars dominates (e.g., Veilleux et al. 2005, 2020). After star-formation ignites, the

* E-mail: alberto.saldana-lopez@astro.su.se

most massive stars emit high-energy photons, drive strong stellar winds, and later explode as energetic supernovae (e.g., [Efstathiou 2000](#); [Hopkins et al. 2012](#)). These processes inject energy and momentum into the interstellar medium (ISM), heating and accelerating gas in the form of galactic outflows (e.g., [Muratov et al. 2015](#); [Nelson et al. 2019](#)). Both at low and high-redshifts, evidence of star-formation driven winds have been found in the cool, absorbing gas traced by the UV transitions (e.g., [Weiner et al. 2009](#); [Steidel et al. 2010](#); [Erb et al. 2012](#); [Martin et al. 2012](#); [Rubin et al. 2014](#); [Roberts-Borsani et al. 2020](#); [Prusinski et al. 2021](#); [Calabrò et al. 2022](#)), as well as in the warmer gas probed by nebular emission (e.g., [Amorín et al. 2012b](#); [Arribas et al. 2014](#); [Freeman et al. 2019](#); [Gallagher et al. 2019](#); [Swinbank et al. 2019](#); [Concas et al. 2022](#); [Reichardt Chu et al. 2022](#); [Marasco et al. 2023](#); [Llerena et al. 2023](#); [Weldon et al. 2024](#)). Outflows are ubiquitous in local, compact starburst galaxies with intense star-formation activity (e.g., [Heckman 2002](#); [Reichardt Chu et al. 2025](#)), showing velocities of hundreds of km s^{-1} (e.g., [Martin 2005](#); [Chisholm et al. 2015](#); [Xu et al. 2022b](#)), and mass outflow rates comparable to their SFR (e.g., [Rupke et al. 2005](#); [Heckman et al. 2015](#)). The incidence of outflows plays a major role in galaxy populations near the Cosmic Noon ([Newman et al. 2012](#); [Genzel et al. 2014](#); [Davies et al. 2019](#); [Förster Schreiber et al. 2019](#)), partially due to the increase in the cosmic star-formation rate density (see [Förster Schreiber & Wuyts 2020](#), for a review).

Galactic outflows have the ability to enrich the Circumgalactic Medium (CGM) with metals (e.g., [Muratov et al. 2017](#); [Chisholm et al. 2018](#); [Hamel-Bravo et al. 2024](#)). In a virialized system, the escape velocity is inherently linked to the dynamical mass (e.g., [Heckman et al. 2000](#); [Arribas et al. 2014](#)) of the galaxy. Therefore, the shallow potential wells in low-mass galaxies enable their outflows to more easily escape (e.g., [Xu et al. 2023](#); [Carniani et al. 2024](#)). The dynamical mass also determines the rotational velocity of the gas particles within the galaxy. Observations of star-forming galaxies at $0 \leq z \leq 3$ (e.g., see [Übler et al. 2019](#), and references therein) suggest an exponential increase in gas turbulence with look-back time, which may eventually prevent the formation of rotationally-supported structures in high- z systems (e.g., [Pillepich et al. 2019](#)). The dynamical mass, together with galactic feedback (e.g., [Krumholz et al. 2018](#)), fundamentally impacts the morphology and mass assembly history of galaxies (e.g., [Cappellari et al. 2006](#); [Belli et al. 2014](#)). However, empirical constraints on the gas kinematics and the dynamical mass of galaxies beyond Cosmic Noon are limited to a few number of studies (e.g., see [Parlanti et al. 2023](#); [de Graaff et al. 2024](#)).

Prior to the commissioning of *JWST*, our knowledge about ionized gas flows in galaxies was vastly restricted to $z < 4$, as either the UV spectral features become too faint beyond these distances, or the emission lines in the rest-optical wavelength range become inaccessible from the ground. Luckily, and thanks to the sensitivity and spectral coverage of the NIRSpec instrument (e.g., [Jakobsen et al. 2022](#)) on board of the James Webb Space Telescope (e.g., [McElwain et al. 2023](#); [Rigby et al. 2023](#)), we are now able to study the properties of gas flows and their host galaxies in the first few Gyr of cosmic history (e.g., [Tang et al. 2023](#); [Xu et al. 2023](#); [Carniani et al. 2024](#); [Roy et al. 2024](#); [Zhang et al. 2024](#)). Studying both the dynamical properties of galaxies and the demographics of outflows at high-redshift is crucial to test the validity of the feedback models (e.g., [Pandya et al. 2021](#)) and the formation of structures at early stages of galaxy evolution (e.g., [Kohandel et al. 2024](#)). In this work, we make use of high-resolution NIRSpec spectroscopy to study the kinematics of the ionized gas, the dynamical mass, and the outflow

properties of a sample typically luminous galaxies beyond Cosmic Noon.

The paper is organized as follows. In Section 2, we present the GO1871 observations and data reduction, spectral energy distribution (SED) and morphological fitting. We also describe the line emission and outflow modeling. In Section 3, we present an overview of the properties of the sample in the context of other measurements at high- z . Section 4 reads about the velocity dispersion of the ionized gas and the dynamical mass of galaxies beyond Cosmic Noon. Section 5 focuses on the properties of the outflow candidates identified in our high- z galaxy sample, concretely on outflow velocities, mass outflow rates, and mass loading factors. In the same section, we link the properties of the outflow to the dynamical mass, aiming to study the efficiency of the feedback and subsequent enrichment of the CGM. We list our conclusions in Section 6.

Every discussion across the manuscript is accompanied by comparisons with other samples in the literature, and sometimes with numerical predictions from cosmological simulations. Throughout we assume a cosmology of $\{H_0, \Omega_M, \Omega_\Lambda\} = \{70 \text{ km s}^{-1} \text{ Mpc}^{-1}, 0.3, 0.7\}$, speed of light $c = 2.99792 \cdot 10^5 \text{ km s}^{-1}$ and the AB magnitude system ([Oke & Gunn 1983](#)).

2 DATA AND METHODS

2.1 The GO1871 *JWST* program

The GO1871 Cycle 1 (PI: Chisholm) program was initially targeted at investigating 20 high redshift star-forming galaxies in the GOODS-North (GOODS-N) field, using *JWST* NIRSpec Micro-Shutter ([McElwain et al. 2023](#); [Rigby et al. 2023](#)) in both G235H/F170LP and G395H/F290LP gratings. The goal of the project was to study the production and escape of ionizing photons during the Reionization era. With this aim, we used high-resolution gratings to capture velocity-resolved Mg II emission profiles at 2800\AA rest-frame, which provide important insights into the neutral gas and escape of ionizing radiation from galaxies (f_{esc} [Henry et al. 2018](#); [Chisholm et al. 2020](#); [Xu et al. 2022a](#)). The main results of this program were presented in [Gazagnes et al. \(2024\)](#), where we studied the contribution of two luminous galaxies to the ionizing photon budget during the Epoch of Reionization (EoR), by placing indirect constraints on f_{esc} using the Mg II line.

These galaxies were selected from an original catalog of 1,036 sources ([Finkelstein et al. 2015](#); [Bouwens et al. 2015](#)) using deep Hubble Space Telescope (HST) F160W observations to identify $z \geq 5$ targets, with either photometric or spectroscopically confirmed redshifts ([Jung et al. 2020](#)). From the parent sample, we kept candidates with $m_{\text{F160W}} \leq 28$ AB magnitudes and significant (3σ) *Spitzer* $4.5 \mu\text{m}$ detections, ensuring that they are EoR galaxies but bright enough to detect Mg II in emission. We used the 100 mas pixel-scale Complete Hubble Archive for Galaxy Evolution (CHARGE; [Fujimoto et al. 2022](#); [Kokorev et al. 2022](#))¹ imaging in the *HST* F160W band to define the source locations. Centering the MSA footprint on a bright $z = 7.5$ Ly α emitter in GOODS-N ([Finkelstein et al. 2013](#); [Hutchison et al. 2019](#); [Jung et al. 2020](#)), left us with a final sample of 20 star-forming galaxies successfully allocated inside the micro-shutters.

¹ <https://gbrammer.github.io/projects/charge/>

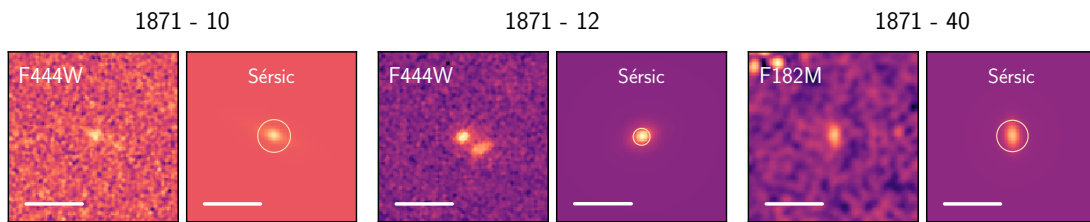


Figure 1. Examples of NIRCam data and morphological modeling for GO1871 gas-flow candidates. For each galaxy the ID is given, and the *left panels* show 3×3 arcsec² cutouts in the corresponding NIRCam band, with the white bar spanning 1 arcsec length. Sérsic or point-like best-fit models are shown in the *right panels*, using the PYSERSIC code (see Sect. 2.2). Yellow circles indicate the best-fit effective radius (r_e).

2.2 NIRCam photometry

2.2.1 NIRCam data

In addition to our dedicated NIRSpectroscopy, *JWST* NIRCam (Rieke et al. 2023) observations of the GOODS-N field were conducted as part of the First Reionization Epoch Spectroscopically Complete Observations (FRESCO; Oesch et al. 2023). These included medium-band observations in the F182M and F210M bands (4,456 and 3,522s, respectively) and shallower F444W broad-band imaging (934s), aiming for a point-source 5σ detection of 28.2mag in all exposures. The GOODS-N field also benefits from extensive multi-wavelength data, including deep *HST* and other ground- and space-based observations (e.g., Barro et al. 2019).

The FRESCO NIRCam images were processed following the methods in Endsley et al. (2023), using the *JWST* Science Calibration Pipeline² (v1.11.3) and the `jwst_1106.pmap` reference file. All NIRCam mosaics were resampled onto the same World Coordinate System at $30 \text{ mas pixel}^{-1}$. Images were convolved to match the point-spread function (PSF) of the F444W filter, using empirically derived PSFs from GAIA confirmed stars in the FRESCO mosaics. Finally, the photometry was calculated in elliptical Kron apertures after employing a neighbor subtraction algorithm following Endsley et al. (2023, 2024).

2.2.2 SED fitting and morphological modeling

We derived constraints on the SED properties (namely stellar masses, M_* , and star-formation histories, SFHs) of the 20 on-slit GO1871 galaxies by fitting the *HST* plus FRESCO NIRCam photometry with the Bayesian Analysis of Galaxies for Physical Inference and Parameter ESTimation code (BAGPIPES³; Carnall et al. 2018). M_* and SFHs were determined by constraining the underlying rest-frame UV to optical continuum, as well as the strength of the prominent [O III] and H β lines in the redder part of the spectra. We accounted for the contribution from the emission lines by including the observed emission line equivalent widths (EW) from the NIRSpectroscopy (see subsection 2.3) in the BAGPIPES fits.

BAGPIPES uses the updated Bruzual & Charlot (2003) stellar population synthesis templates with Kroupa (2001) stellar initial mass function, and includes nebular continuum and emission lines by processing the stellar emission through CLOUDY v17.00 (Ferland et al. 2017). In fitting the data, we adopted the “bursty continuity” prior for the SFHs (following Tacchella et al. 2022), motivated by the large optical equivalent widths of strong emission lines in

GO1871 spectra (e.g., Atek et al. 2022). We allowed for a broad range of stellar masses, metallicities, and ionization parameters, applying log-uniform priors to all three physical properties. We adopt a Calzetti et al. (2000) dust-attenuation law with the V-band optical depth allowed to vary between $A_V = 0.001 - 2$ mag. The redshift was fixed to the NIRSpectroscopy value (see below). The resulting SED-derived UV magnitudes, stellar masses, and SFRs of the full sample are listed in Table A1 of the Appendix.

Finally, we made use of the PYSERSIC⁴ software to characterize the morphology of every galaxy (Pasha & Miller 2023). We first produced 3×3 arcsec² cutouts from the PSF-matched F182M, F210M and F444W FRESCO images. We then used PYSERSIC to fit 2D Sérsic profiles to the light distribution of the F444W band, accounting for PSF convolution and assuming flat priors for the Sérsic parameters. If a galaxy was not detected at 3σ in F444W, we used the F182M or F210M cutouts instead (this happens for seven out of 20 galaxies in the sample). PYSERSIC returns the best-fit values for the amplitude, effective radius (r_e), Sérsic index (n), ellipticity (q) and position angle (PA), using Bayesian Inference. In four cases, r_e was smaller than the PSF FWHM (e.g., 0.145 arcsec for F444W). Consequently, we considered these galaxies to be *unresolved*, and modeled their light profile assuming a point-like morphology instead, by re-scaling the intensity of the PSF to match the galaxy flux.

Figure 1 shows examples of NIRCam data and the corresponding Sérsic or point-source best-fit models for a selection of GO1871 galaxies (gas-flow candidates in the next Section). It is worth noticing that the 1871 – 12 system, first published in Gazagnes et al. (2024), comprises two galaxies separated by 0.36 pMpc. Hereafter, we will only consider the morphology of the brighter (NE) component, shown at the center of the F444W cutout in the former figure. Likewise, source 1871 – 63 correspond to the intermediate-mass black hole (IMBH) candidate by Chisholm et al. (2024), also part of the GO1871 sample. The results from our morphological modeling can be found in Table A2 of this manuscript.

2.3 NIRSpectroscopy

2.3.1 NIRSpectroscopy data

The NIRSpectroscopy observations were split between the G235H and G395H grating configurations. G235H, targeting the rest-frame 2550–3500 Å for galaxies within the EoR ($5.5 < z < 9.5$), focused on the Mg II emission lines and received a longer exposure time: 53,044s (14.7 hours) across 36 exposures. The G395H grating, covering 3400–6000 Å at the same redshift, contains brighter optical

² <https://jwst-pipeline.readthedocs.io/en/latest/index.html>

³ <https://bagpipes.readthedocs.io/en/latest/>

⁴ <https://pysersic.readthedocs.io/en/latest/index.html>

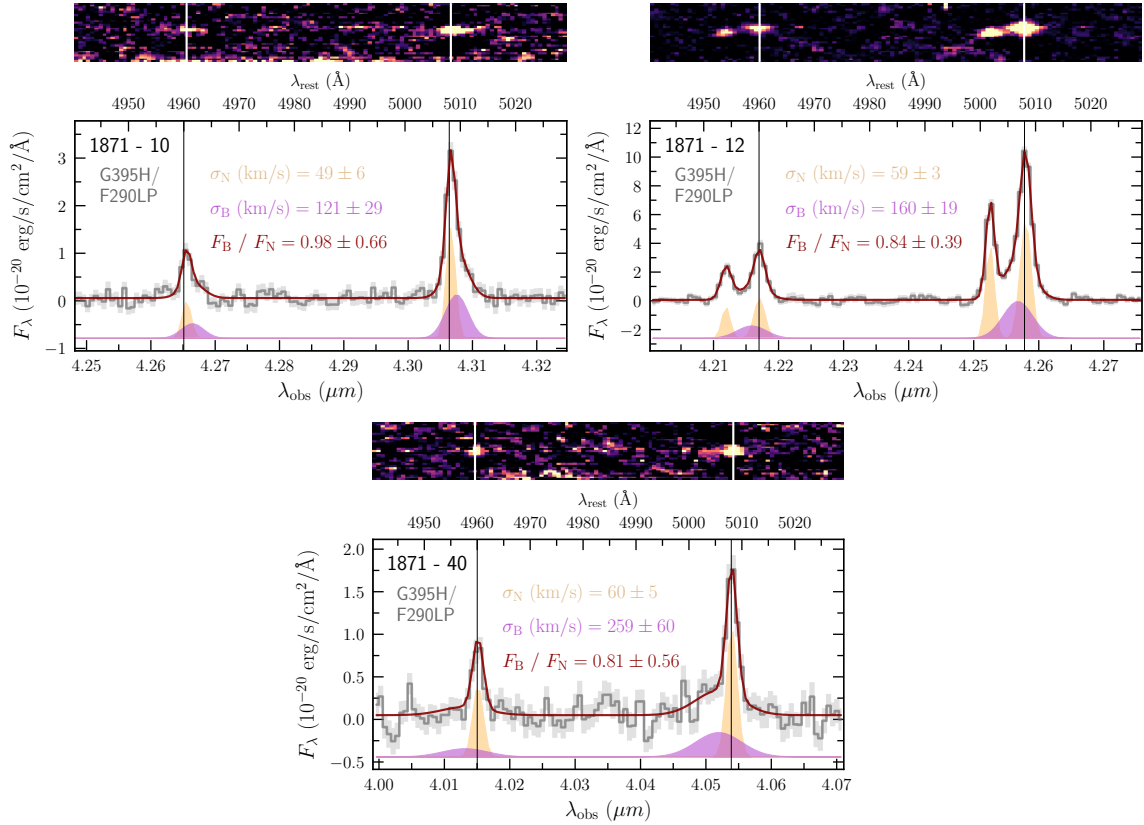


Figure 2. Examples of NIRSpec spectra for GO1871 gas-flow candidates. Each panel contains the high-resolution G395H / F290LP 2D (*top*) and extracted 1D spectra (*bottom*), showing the [O III] $\lambda\lambda 4960, 5008$ doublet (indicated by white and black vertical lines at the top and bottom of each panel, respectively). The red lines show the best simultaneous fits to both emission lines plus the continuum (see Sect. 2.3). The narrow, yellow Gaussians reproduce the static component of the ionized gas, and purple Gaussians model the gas-flows over the broad wings of the [O III] lines. Best-fit values for the velocity dispersion of each component (σ_{narrow} , σ_{broad}), as well as the broad-to-narrow flux ratios ($F_{\text{B}}/F_{\text{N}}$) are labeled in the insets. Galaxy 1871 – 12 has an associated fainter companion at 0.36 pMpc (Gazagnes et al. 2024): two pairs of [O III] doublets are clearly resolved in the NIRSpec spectra.

emission and required less integration time: 9,716s (2.7 hours) over 6 exposures. Both configurations used NRSIRS2 readout mode and the standard three-shutter nod pattern for background subtraction.

For data reduction, we processed the NIRSpec data with the MSAEXP⁵ v0.8.4 Python package (Brammer 2023), using the `jwst_1235.pmap` reference file. This applied $1/f$ noise correction, snowball detection, bias removal using a median filter, and noise re-scaling from empty parts of the exposure. MSAEXP also performed parts of the Level 2 JWST calibration pipeline, including manual background subtraction based on 2D slit cutouts. The pipeline used the Space Telescope Science Institute’s v1.14.0 standard for Level 2 calibration, with wavelength calibration based on the NIRSpec instrument model (Lützendorf et al. 2022). All exposures were co-added without slit-loss correction. Four out of 20 sources originally within the MSA micro-shutters show neither continuum nor line detections, and therefore are removed from the final working sample. Our final working sample then constitutes of 16 galaxies. We refer the reader to Chisholm et al. (2024) and Gazagnes et al. (2024) for more details about the NIRSpec data reductions of this program.

2.3.2 Emission line measurements

From Mg II at 2800Å to the [S II] doublet at 6730Å a suite of nebular lines are detected in the blue and red portions of the combined NIRSpec GO1871 spectra (G235H and G395H), covering the rest-frame optical wavelengths at the redshift of our observations. Here is a list of the main features, where the name of each ion is followed by the ionization state as well as the rest-frame wavelength (in vacuum): [O II] $\lambda\lambda 3727, 3729$, [Ne III] $\lambda 3869$, H δ $\lambda 4102$, H γ $\lambda 4341$, H β $\lambda 4862$, [O III] $\lambda\lambda 4960, 5008$, [N II] $\lambda\lambda 6549, 6585$, H α $\lambda 6564$, [S II] $\lambda\lambda 6718, 6732$.

We fit individual Gaussian profiles to each line emission in the observed f_{λ} frame, following:

$$F_{\lambda} = C + \frac{F_{\text{tot}}}{\sigma_{\lambda}\sqrt{2\pi}} \exp\left(-\frac{(\lambda - \lambda_0)^2}{2\sigma_{\lambda}^2}\right), \quad (1)$$

where C is the local continuum level, assumed to be a positive constant for each transition. The continuum C , amplitude F_{tot} (integrated flux of the line), observed central wavelength λ_0 (in μm), and observed velocity dispersion σ_{λ} (μm) are free parameters within the fit. During the fit we assumed uniform priors on all free parameters. All of the spectroscopic multiplets are resolved at the resolution of our observations (nominal resolving power of the H -gratings is $R \approx 3,000$). In this vein, nebular lines coming from the same ionized gas should have comparable velocity dispersions, but the

⁵ <https://github.com/gbrammer/msaexp>

wavelength-dependent resolution of NIRSpec prevents us from trying their σ_λ together without significant forward modeling of the delivered NIRSpec spectral resolution. Instead, only lines within resolved multiplets that are close in wavelength (and of the same ion) are fitted simultaneously by assuming the same velocity dispersion for all constituents (in wavelength space, for example [O III] λ 4960 and 5008), fixing the relative λ_0 ratio according to the vacuum wavelengths listed above. The contribution from the stellar absorption in the H I lines is neglected in our analysis, as we expect this to be low given the high EW of the Balmer lines (e.g., González Delgado et al. 1999).

We employ the Python package LMFIT⁶ (Newville et al. 2016) to recover the solution which minimizes the reduced χ^2 value. Errors on the line profile parameters are estimated by perturbing observed F_λ fluxes using a normal distribution with a mean of zero and equal to the 1σ error of the flux density for the standard deviation at every pixel, then re-fitting the lines over 1000 iterations per spectrum. The best-fit parameters are taken as the median of each distribution, and the uncertainties correspond to the 0.16 and 0.84 quantiles. For non-detections, we report the 1σ value as upper limits in the line flux.

In Section 3 (see also Table A1), the intensity ratios of the bright optical lines in the GO1871 sample will be compared against other samples in the literature. The merging nature of 1871 – 12 is clearly revealed by the presence of double [O III] profiles in the NIRSpec spectra of this source (Fig. 2). Hereafter, we will only use the line emission of the brighter (NE) galaxy in the system because this is the only component with clear outflow signatures. Finally, we note that the emission line ratios reported in this work are fully compatible with the ones in Gazagnes et al. (2024) for this galaxy component. Similarly, our emission line measurements are compatible with the values presented in Chisholm et al. (2024) for the IMBH candidate.

2.3.3 Identifying gas flows

The imprint of inflows and outflows of ionized gas on the profile of nebular emission lines is in the form of spectral broadening of the emission line wings (e.g., Heckman et al. 1981; Veilleux 1991). Our GO1871 observations are ideal to unveil the presence of inflowing or outflowing gas in the $z \geq 5$ Universe due to the following reasons. First, they target sufficiently bright emission lines, such as [O III] λ 5007 or H α , the same lines traditionally used to study the kinematics of ionized gas in galaxies and AGNs at lower z 's (e.g., Villar-Martín et al. 2011; Amorín et al. 2012b; Arribas et al. 2014; Harrison et al. 2014; Gallagher et al. 2019; Revalski et al. 2021; Ruschel-Dutra et al. 2021; Reichardt Chu et al. 2022; Marasco et al. 2023; Flury et al. 2023; Amorín et al. 2024; Reichardt Chu et al. 2025). Second, the spectral resolution of G1871 observations ($\approx 30 \text{ km s}^{-1}$) is high enough to separate the gas flow component from the static emission, with typical line widths of $\approx 60 \text{ km s}^{-1}$.

These broad wing gas-flow features have been traditionally studied through a variety of methods: from non-parametric (also called *empirical*) methods (e.g., Veilleux et al. 2005) and detailed numerical models (e.g., Krumholz et al. 2017), to the inclusion of additional components in the form of Gaussian (e.g., Pelat & Alloin 1980; Pelat et al. 1981), power-law (e.g., Komarova et al. 2021), Gauss-Hermite (e.g., Riffel 2010) or even semi-analytic, physically motivated functions to describe the line profile (e.g.,

Flury et al. 2023). Due to the limited S/N and resolution of our NIRSpec spectra, we search for gas flow signatures by fitting the profiles of the bright [O III] λ 4960, 5007 doublet using a simple, 2-Gaussian component approach.

In this formalism, an additional Gaussian (name *broad*) is added to the (often brighter) emission coming from the bulk of the static ionized gas (*narrow*), as in:

$$F_\lambda = C + \frac{F_{\text{tot}}^{\text{narrow}}}{\sigma_\lambda \sqrt{2\pi}} \exp\left(-\frac{(\lambda - \lambda_0^{\text{narrow}})^2}{2\sigma_\lambda^2}\right) + \frac{F_{\text{tot}}^{\text{broad}}}{\sigma_\lambda \sqrt{2\pi}} \exp\left(-\frac{(\lambda - \lambda_0^{\text{broad}})^2}{2\sigma_\lambda^2}\right), \quad (2)$$

where $F_{\text{tot}}^{\text{broad}}$, λ_0^{broad} and $\sigma_\lambda^{\text{broad}}$ correspond to the integrated flux, central wavelength and velocity dispersion of the gas flow, respectively. We force $\sigma_\lambda^{\text{broad}} \geq 1.5 \times \sigma_\lambda^{\text{narrow}}$, so that the velocity dispersion of the gas-flow component is at least 50 per cent larger than the static one. For both narrow and broad components, the velocity dispersion of lines from the same ion that are close in wavelength (i.e., part of the same multiplet) were tied together (e.g., [O III] λ 4560 and 5008).

The presence of gas flows in each galaxy (see e.g., Carniani et al. 2024) is determined based on the statistical preference of two Gaussians against a single Gaussian fit. For a galaxy to be considered as a gas flow candidate (following Xu et al. 2023), we require the *Akaike Information Criterion* (AIC) to be reduced at least by five ($\Delta\text{AIC} \leq 5$), and a signal-to-noise ratio (S/N) for the integrated flux of the broad component to be $S/N \geq 3$. AIC has a smaller penalty for the number of free parameters than the *Bayesian Information Criteria* (BIC), and therefore it may include weaker gas-flow signatures. By imposing these criteria, we make sure that our gas-flow candidates are robust, where the resulting χ^2_ν and BIC both decrease at the same time. This way, we found five gas-flow candidates out of 16 galaxies with [O III] observations in GO1871 (details in Sect. 5). We do not detect gas flow features in any other transition than [O III]. This is most likely be due to S/N limitation, as [O III] λ 5008 this is brightest transition in our GO1871 spectra.

Figure 2 shows examples of NIRSpec G395H / F290LP spectra for some of the gas-flow candidates in this work, highlighting the *outflow* and *static* Gaussian best-fit components of the [O III] lines (purple and yellow, respectively). The broad-to-narrow amplitude ratios, as well as other secondary gas-flow parameters, are collected in Table A3 of this paper.

3 SAMPLE OVERVIEW

The GO1871 working sample is composed of 16 moderately faint ($M_{\text{UV}} = -19$ to -21 AB) star-forming galaxies at $z = 4 - 7.6$, with a median spectroscopic redshift of $\langle z_{\text{spec}} \rangle = 6.8$. Out of these 16 galaxies, 12 (75 per cent of the sample) are EoR galaxies in the redshift range $6 \leq z \leq 8$ and among those, all except one (1871 – 912) are fainter than the characteristic $M_{\text{UV}}^* = -21.2$ at $z \approx 7$ (see Bouwens et al. 2021). Figure 3 depicts a summary of the physical properties of GO1871 galaxies, with the top-left panel showing the UV magnitude versus redshift. The IMBH candidate by Chisholm et al. (2024) and the gas-flow candidates of this work, are highlighted with different symbols (see legend).

Balmer decrements were used to estimate the amount of (nebular) dust attenuation in GO1871 galaxies. From H α to H δ , we computed every possible Balmer line ratio, and kept those where

⁶ <https://lmfit.github.io/lmfit-py/index.html>

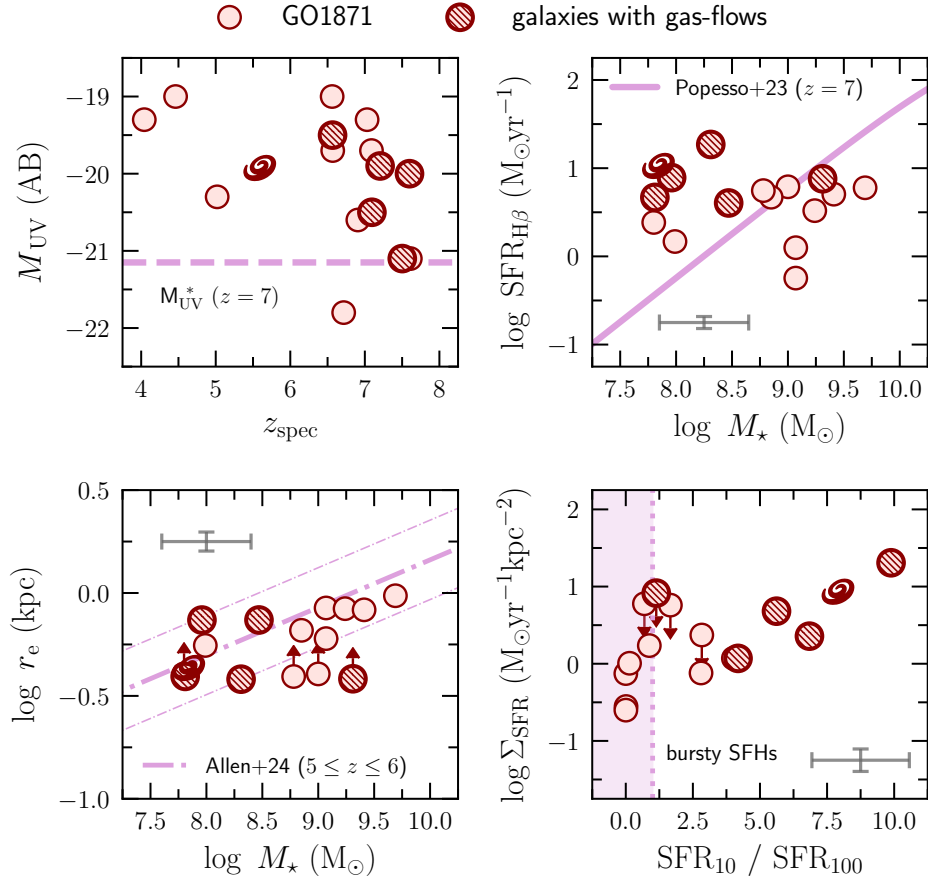


Figure 3. Overview of physical properties for GO1871 galaxies. Hatched symbols indicate gas-flow candidates, and the IMBH candidate from Chisholm et al. (2024) is displayed with a spiral. *Top-left:* UV magnitude versus redshift. The dashed line shows the characteristic M_{UV}^* for $z = 7$ galaxies (Bouwens et al. 2021). *Top-right:* SFR (from $H\beta$) as a function of stellar mass, together with the star-forming main sequence at $z = 7$ from Popesso et al. (2023). *Bottom-left:* rest-optical size-mass relation, as traced by the effective radius (r_e) in comparison with the Allen et al. (2024) best-fit relation at $5 \leq z \leq 6$ (dashed-dotted). *Bottom-right:* SFR surface-density (Σ_{SFR}) versus burstiness parameter (SFR_{10}/SFR_{100}), defined as the ratio between SFRs averaged over 10 and 100 Myr. The properties of GO1871 galaxies are representative of typical high- z galaxies in the EoR.

both lines were detected. The observed Balmer ratios were then compared against theoretical expectations from Case B recombination (Storey & Hummer 1995), although we acknowledge that deviations from Case B might be expected (e.g., McClymont et al. 2024; Scarlata et al. 2024) if the electron densities drastically increase with redshift (e.g. Isobe et al. 2023; Reddy et al. 2023). As a result, all but two galaxies within the GO1871 sample show *negligible* amounts of dust attenuation ($E_{B-V} \leq 0.05$, i.e., the measured ratios are consistent with Case B at 1σ). For the remaining two galaxies (1871-29, 1871-545) we get $E_{B-V} = 0.049, 0.210$ mag., and their line fluxes were corrected by this amount assuming the Reddy et al. (2015) extinction law.

SFRs were derived from the $H\beta$ luminosity adopting a Kroupa (2001) IMF, as in Kennicutt & Evans (2012). SFRs range $SFR_{H\beta}/M_{\odot}\text{yr}^{-1} = 0.3 - 30$ (consistent with SFR_{10} from SED fitting), with SED-derived stellar masses (Sect. 2.2) of $\log M_{\star}/M_{\odot} = 7.75 - 9.75$. The SFR versus M_{\star} diagram (top-right panel of Fig. 3) reveals most of GO1871 galaxies are highly star-forming, where all but five galaxies in the sample fall either well-above or on top of the SF main sequence (MS) at $z = 7$ (Speagle et al. 2014; Popesso et al. 2023). Notably, most of the galaxies with detected broad components (hatched circles) lie significantly above the SFMS. Con-

cretely, the IMBH and the five gas-flow candidates have low masses ($\log M_{\star}/M_{\odot} \leq 8.5$) and most show positive $\Delta MS \geq 0.5$ dex.

The effective radii of GO1871 galaxies are in the range of $r_e = 0.08 - 0.18$ arcsec, or 400–960 pc, with 12 out of 16 galaxies being resolved by the NIRCcam imaging. The so-called size-mass relation is presented in the bottom-left panel of Fig. 3, with the recent Allen et al. (2024) relation at $5 \leq z \leq 6$ overlaid. Our galaxies fall within the observational uncertainties of this relation. In the same manner, star-formation rate surface densities ($\Sigma_{SFR}/M_{\odot}\text{yr}^{-1}\text{kpc}^{-2} = 0.3 - 20$) were computed by dividing half of the $H\beta$ -derived SFRs (as only half the flux is contained within r_e) by the area given by a circumference of r_e in radii, as in:

$$\Sigma_{SFR} = \frac{SFR_{H\beta}}{2\pi r_e^2}, \quad (3)$$

Our custom BAGPIPES SED fitting allows us to compute SFRs over different time spans for each galaxy. Commonly used time bins are SFR_{10} and SFR_{100} , averaged over the last 10 and 100 Myr, respectively (Endsley et al. 2023). By definition, SFR_{10} traces the most recent (instantaneous) SFR events and closely follows the values derived from the $H\beta$ recombination line ($SFR_{H\beta}$). Likewise, SFR_{100} is largely driven by the luminosity of the UV continuum,

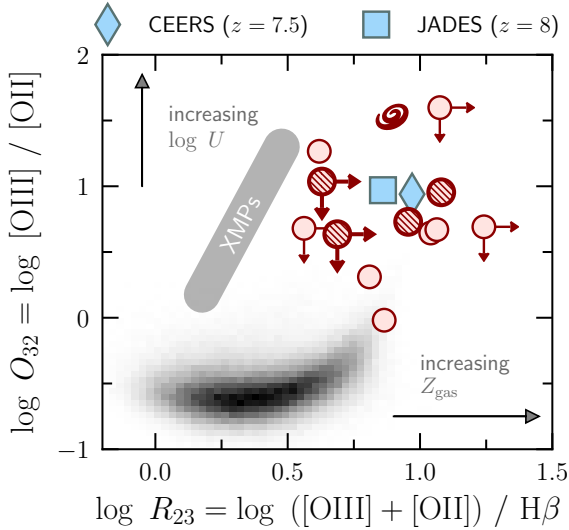


Figure 4. O_{32} (a proxy of the ionization state) versus R_{23} . The blue diamond and square show the average for $z = 7-8$ galaxies from the CEERS (Sanders et al. 2023) and JADES surveys (Cameron et al. 2023). The grey 2D histogram in the background shows the density of SDSS galaxies at $z \approx 0$ (e.g., Brinchmann et al. 2008). The space of parameters occupied by the compilation of extremely metal-poor galaxies (XMPs) from Izotov et al. (2024), is illustrated with a grey shaded band. With high ionization parameters and low metallicities, high- z star-forming galaxies share the locus in this diagram with local analogs such as Green Pea, Blueberries and EELGs.

and it traces a more continuous level of the the SFR over time. As a consequence, the ratio between both can be interpreted as a proxy of recent burstiness in the SFH of galaxies (Atek et al. 2022). The last panel of Fig. 3 displays the positive correlation between the Σ_{SFR} and this ‘burstiness’ parameter. Interestingly, the Chisholm et al. IMBH and most of our gas-flow candidates show high Σ_{SFR} (highly star-forming and compact) as well as recent bursts of star-formation ($\text{SFR}_{10}/\text{SFR}_{100} > 1$).

With the advent of *JWST*/NIRSpec, we have access for the first time to optical emission-line diagrams at redshifts higher than $z = 4$ (e.g., Schaerer et al. 2022; Trump et al. 2023; Trussler et al. 2023). We now use the (attenuation corrected) $O_{32} = [\text{O III}]\lambda 5007/[\text{O II}]\lambda 3727,29$ versus $R_{23} = ([\text{O III}]\lambda 5007 + [\text{O II}]\lambda 3727,29)/H\beta$ diagram to investigate the ionization state of the ionized ISM in our sample of $4 \leq z \leq 8$ galaxies (see Table A1). O_{32} is a direct proxy of the degree of ionization (e.g., Kewley & Dopita 2002; Kobulnicky & Kewley 2004; Nakajima & Ouchi 2014), while R_{23} is primarily sensitive to the gas-phase metallicity with a secondary dependency on the ionization parameter (e.g., Maiolino et al. 2008; Curti et al. 2017, 2020).

Figure 4 shows the $O_{32} - R_{23}$ diagram for GO1871 galaxies. Our sample of high- z galaxies show overall high O_{32} and R_{23} values ($\log O_{32} = 0.5 - 2$, $\log R_{23} = 0.5 - 1.5$) compared to the bulk of nearby SDSS galaxies (grey shaded 2D histogram, e.g., Brinchmann et al. 2008), compatible with the findings of the literature at Cosmic Noon (e.g., Strom et al. 2017). These high O_{32} and R_{23} are in agreement with other individual *JWST* observations at similar redshifts (e.g., Saxena et al. 2024; Mascia et al. 2023), with a tendency for high- z galaxies to move towards the high ionization locus in almost every emission line ratio diagnostic diagram (Shapley et al. 2023; Backhaus et al. 2024). As a comparison example, in Fig. 4 we also show stacked measurements of $z \geq 7$ galaxies

from the JADES and CEERS surveys (blue symbols, see Cameron et al. 2023; Sanders et al. 2023). In addition, GO1871 galaxies share ionization parameters and excitation ratios with nearby Green Peas (e.g., Cardamone et al. 2009; Amorín et al. 2012a; Jaskot & Oey 2013), Blueberries (e.g., Yang et al. 2017), Extreme Emission Line Galaxies (EELG, e.g., Atek et al. 2011; Tang et al. 2019; Onodera et al. 2020; Berg et al. 2022) and strong Lyman Continuum Emitters (e.g., Izotov et al. 2018, 2020; Nakajima et al. 2020; Flury et al. 2022) at low and/or intermediate redshifts. Extremely metal-poor galaxies (XMPs), conversely, move to the left-hand side part of this diagram (e.g., Izotov et al. 2021, 2024), as the metal lines become weaker (see grey shaded band in the plot).

Taking altogether, these results reveal a coherent picture by which the typical high- z galaxy seems to host a highly ionized and moderately metal-poor ISM with low dust attenuation (cf., Nakajima et al. 2023). As widely studied in the literature, these conditions are might be driven by the increased hardness of the ionizing spectra in low-metallicity stellar populations (e.g., Nakajima et al. 2016; Steidel et al. 2016; Onodera et al. 2016; Sanders et al. 2016; Strom et al. 2017, 2018; Sanders et al. 2021; Runco et al. 2021; Papovich et al. 2022). Last but not least, it is worth noticing the extreme O_{32} observed in the IMBH candidate of Chisholm et al. (2024). Reproducing the complete nebular structure of this galaxy, including transitions such as $[\text{Ne V}]$ and He II , required invoking both massive stars and accretion on to a black hole. For the rest of the GO1871 galaxies we do not observe evidence of AGN largely contributing to the observed properties of the galaxies, neither through broad line regions (BLRs) nor high-ionization lines. These observations suggest that stellar feedback may dominate the baryon cycle of GO1871 galaxies. We stress, however, that the presence of low-mass black holes leading to a possibly subdominant contribution of AGN feedback, cannot be empirically ruled out.

4 DYNAMICAL MASSES IN HIGH-REDSHIFT GALAXIES

The atmospheric sky transmission prevents ground-based telescopes to observe rest-frame optical emission lines beyond $z = 4$. Luckily, the NIRSpec instrument on board of *JWST* (Jakobsen et al. 2022) offers both the spectral coverage and instrumental resolution to resolve the ionized gas kinematics of star-forming galaxies beyond this redshift.

4.1 Velocity dispersion of the ionized gas

Our Gaussian fits to the GO1871 spectra reveal velocity dispersions of the order of σ (km s^{-1}) $\approx 50-100$ for $[\text{O III}]\lambda 5008$, aligning, for instance, with previously reported values for the narrow component in nearby starburst galaxies (e.g., Chávez et al. 2014; Amorín et al. 2024). We use the publicly available *MSAFIT*⁷ python package (de Graaff et al. 2024) to estimate the NIRSpec spectral resolution for every galaxy at the wavelength of the $[\text{O III}]$ line. *MSAFIT* is a forward modeling software that accounts for complexities such as the PSF, source size and location with shutters, shutter geometry, bar shadows and pixelation of the NIRSpec data. It uses the source morphology (r_e, n, q, PA , see Sect. 2.2), the location of the source in the MSA array and its positioning within the slit to compute the *Line Spread Function* (LSF) of the instrument.

⁷ <https://github.com/annadeg/jwst-msafit>

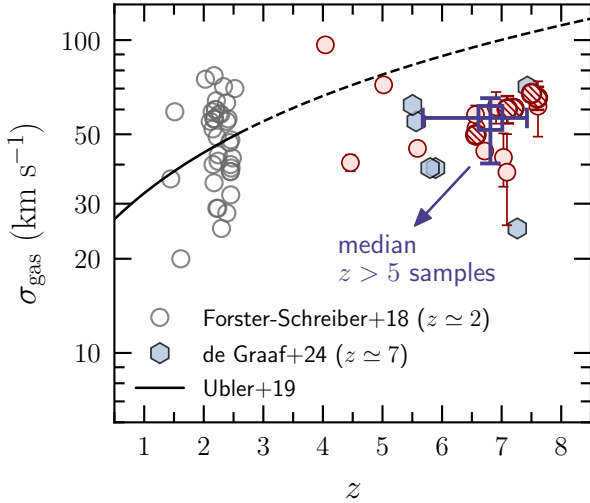


Figure 5. Evolution of the ionized gas velocity dispersion (σ_{gas}) with redshift. Open circles show the measurements from Förster Schreiber et al. (2018) at $z \approx 2$, and the solid (dashed) line indicates the linear fit (extrapolation) by Übler et al. (2019). Other NIRSpect measurements (using O III and H α) at similar redshifts to this work are shown with hexagons (de Graaff et al. 2024). The blue open square gives the median of both NIRSpect samples at $z > 5$, with error bars measuring 0.16 and 0.84 quantiles. Ionized gas in high- z SFGs have comparable velocity dispersions to Cosmic Noon galaxies.

We estimate σ_{res} (km s $^{-1}$) = 29–38 for the velocity dispersion introduced by NIRSpect at observed-frame wavelengths of 5008Å. Then, we correct for the intrinsic velocity dispersion of the ionized gas (σ_{gas}), accounting for instrumental broadening, as,

$$\sigma_{\text{gas}} = \sqrt{\sigma^2 - \sigma_{\text{res}}^2}, \quad (4)$$

resulting in σ_{gas} (km s $^{-1}$) = 38 – 96 (Table A2). GO1871 galaxies seem to have spectroscopically resolved [O III] profiles, in which the observed σ values are broader than the instrument LSF for all systems. Figure 5 shows the ionized-gas velocity dispersions of our sample as a function of redshift. We compare with the near-IR SINS/zC-SINF sample of Förster Schreiber et al. (2018) at $z \approx 2$ and higher stellar masses than this work, and with the NIRSpect results presented in de Graaff et al. (2024), at comparable redshifts and stellar masses.

Ground-based spectroscopic surveys at $z = 0 - 4$ targeting the kinematics of the ionized gas (SAMI: Varidel et al. (2020); MAGPI: Mai et al. (2024); DEEP2: Kassin et al. (2012); KROSS: Johnson et al. (2018); SINS/zC-SINF: Förster Schreiber et al. (2018); KMOS 3D : Wisnioski et al. (2015); Übler et al. (2019); MOSDEF: Price et al. (2020); KDS: Turner et al. (2017)), have demonstrated that the velocity dispersion of star-forming galaxies increases with redshift. To illustrate this behavior, in Fig. 5 we include the analytic fit to the KMOS 3D data ($\log M_{\star}/M_{\odot} = 9 - 11$) at $z \approx 1 - 3$ (solid line, from Übler et al. 2019). Extrapolating this fit to $z = 7$ (dashed line) suggests that the ionized gas was highly turbulent in high- z systems (see the first systematic measurements at $z \geq 4$ with ALMA, e.g., Fraternali et al. 2021; Rizzo et al. 2021; Parlanti et al. 2023; Rizzo et al. 2023). Consistently, prevailing galaxy formation theories predict more turbulent galaxies in the early Universe as an outcome of increase star-formation, merger activity, gravitational instabilities, the accretion of gas from the cosmic web, and stellar feedback (e.g., Krumholz et al. 2018; Pillepich et al. 2019).

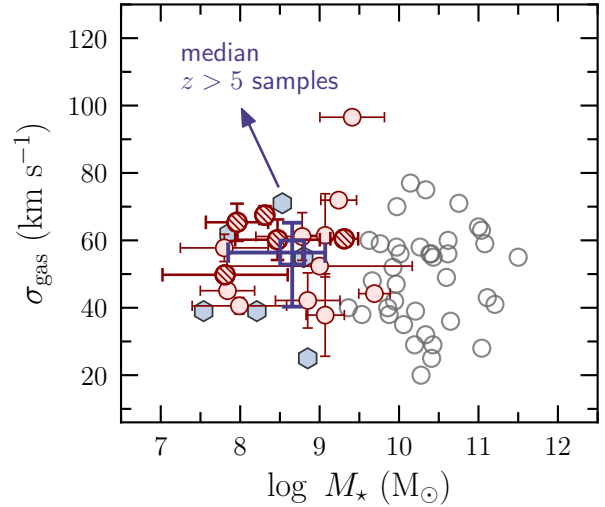


Figure 6. The ionized gas velocity dispersion (σ_{gas}) versus the galaxy stellar mass (M_{\star}). High- z galaxies show stellar masses 1–2 dex lower than the literature data at lower redshifts, and therefore are expected to have a much lower σ_{gas} values. The evolution of σ_{gas} with z at fixed M_{\star} , however, compensates for this effect. Symbols are the same as in Fig. 5.

However, the previously mentioned trend of increasing σ_{gas} with z does not extend to the high- z of our galaxies. Both de Graaff et al. (2024) and our GO1871 measurements report average values of the velocity dispersion comparable to Cosmic Noon galaxies, with an average of $\sigma_{\text{gas}} = 56^{+16}_{-8}$ km s $^{-1}$ between these two samples at $z \geq 5$ (dark-blue square in the Fig. 5). These low σ_{gas} values respect to cosmological predictions seem to be in line with recent findings of rotationally-supported and disc-like structures with JWST (Conselice et al. 2024; Tsukui et al. 2024; Y. Xu et al. 2024; Ferreira et al. 2023, 2022) and ALMA (Rowland et al. 2024), out to much higher redshifts than previously expected (see Kohandel et al. 2024, for a simulation-based work).

According to models (e.g., Ejdetjärn et al. 2022), the stellar mass and SFR are the primary drivers of the ionized-gas velocity dispersion at fixed cosmic time, and observations have established dependencies of increasing σ_{gas} with both increasing M_{\star} and SFR (e.g., Lehnert et al. 2009; Green et al. 2010; Yu et al. 2019). To illustrate this, in Figure 6 we have plotted the estimated σ_{gas} as a function of the galaxy stellar mass, for both high- z (de Graaff et al. 2024, this work) and the Cosmic Noon samples. Although this diagram do not show any apparent correlation, the typical stellar mass of the $z = 7$ samples is 1–2 dex lower than the literature data at lower redshifts, and therefore one would expect the $z = 7$ galaxies to have a factor of ~ 2 lower σ_{gas} than we observe. However, the underlying evolution of σ_{gas} with z at fixed M_{\star} compensates for this effect (e.g., Pillepich et al. 2019), with σ_{gas} increasing by the same factor due to the above mentioned phenomena. The complementary behavior can be seen at lower redshifts. For instance, at fixed $\log M_{\star}/M_{\odot} = 8 - 9$ (similar to the M_{\star} of our sample), Varidel et al. (2020) reported average σ_{gas} as low as ≈ 20 km s $^{-1}$ for $z = 0$ galaxies, while Maseda et al. (2013) measured a mean of ≈ 50 km s $^{-1}$ over a sample of $z = 2$ dwarfs. In conclusion, our observations suggest that the velocity dispersion of ionized gas increases at fixed M_{\star} with increasing redshift.

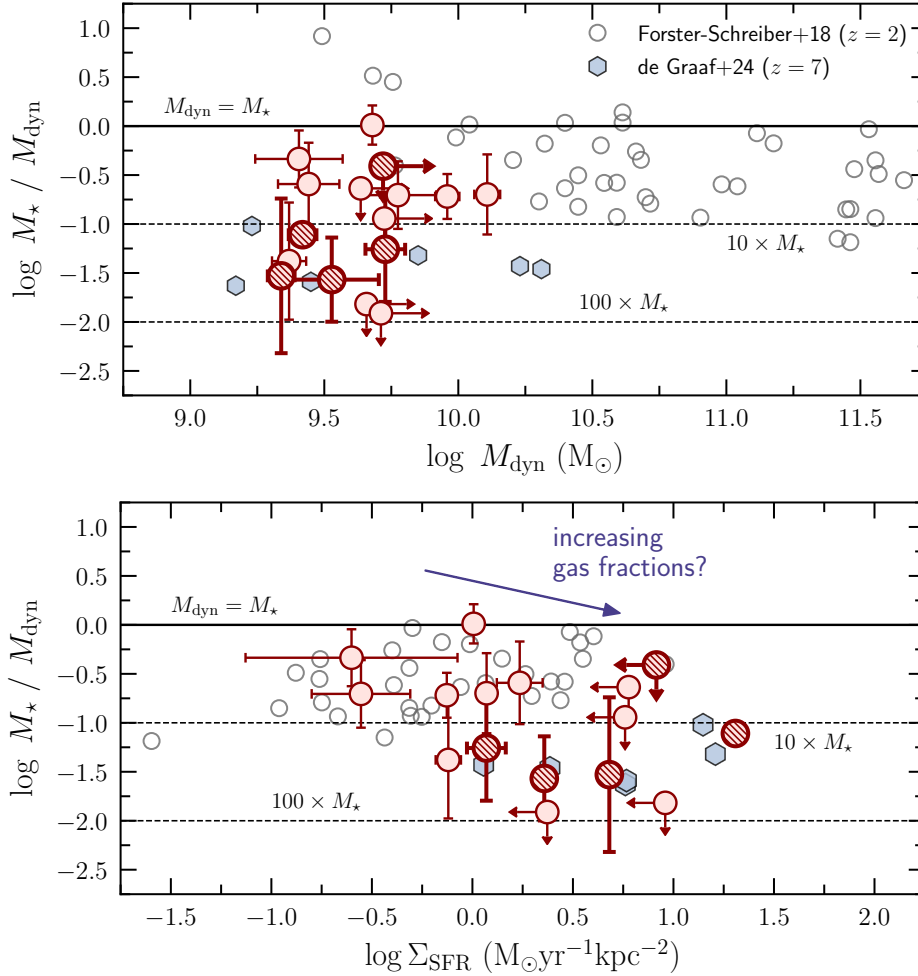


Figure 7. Stellar mass (M_\star) to dynamical mass (M_{dyn}) ratio as a function of dynamical mass (*top*) and SFR surface density, Σ_{SFR} (*bottom*). The solid line follows the $M_{\text{dyn}} = M_\star$ relation, while dashed lines show $\times 10M_\star$ and $\times 100M_\star$. On average, low-mass, high- z galaxies with moderate SFRs exhibit lower M_\star/M_{dyn} ratios and lower dynamical masses than more massive and highly star-forming systems at Cosmic Noon (top figure). This behavior can be attributed to higher gas-mass fractions in high- z systems, as suggested by the tentative correlation found between M_\star/M_{dyn} and Σ_{SFR} (bottom figure). Symbols are the same as in Fig. 5.

4.2 Dynamical and baryonic mass budgets

Taking advantage of the resolved [O III] lines in GO1871 galaxies, we now investigate the relation between the dynamical mass (M_{dyn}) and stellar mass (M_\star). In virialized systems, the mean velocity dispersion of the gas particles is a representation of the average thermal (kinetic) energy, and is therefore linked to the gravitational potential wells responsible for imprinting rotational motions into the gas particles. The mass-equivalent to this gravitational potential is called the *dynamical mass*, and it reflects the addition of the dark and baryonic mass enclosed within a certain radius.

Following Übler et al. (2023) and Maiolino et al. (2024), the dynamical mass (M_{dyn}) can be defined as,

$$M_{\text{dyn}} = K(n) K(q) \times \frac{\sigma_{\text{gas}}^2 r_e}{G}, \quad (5)$$

where $K(n) = 8.87 - 0.831n + 0.0241n^2$ from Cappellari et al. (2006), $K(q) = [0.87 + 0.38 e^{-3.71(1-q)}]^2$ from van der Wel et al. (2022), and n, q, r_e are the Sérsic index, axis ratio and effective radius from our morphological fits to the NIRCcam data (see results in Table A2). Among the uncertainties on the several quantities

involved in the determination of M_{dyn} , the r_e contributes the most to the final error budget. Four out of 16 galaxies are unresolved in the NIRCcam mosaics. For those, we report upper-limits in M_{dyn} by replacing the effective radius with the FWHM of the PSF in the F444W band.

The resulting M_\star/M_{dyn} ratio is plotted as a function of M_{dyn} in the upper panel of Figure 7. The dynamical mass ($\log M_{\text{dyn}}/M_\odot \geq 9.25 - 10.25$) is larger than the stellar mass in both GO1871 and de Graaff et al. samples. Conversely, Cosmic Noon galaxies, having $\log M_{\text{dyn}}/M_\odot \geq 10$ and higher stellar masses, show larger M_\star/M_{dyn} ratios. Because the contribution of dark matter to the mass budget is presumably negligible at these small spatial scales (≤ 1 kpc see e.g., Genzel et al. 2017), the discrepancy between the stellar and dynamical mass is usually attributed to the contribution of the total (ionized+neutral) gas mass to the dynamical mass (M_{gas} , e.g., Erb et al. 2006; Chávez et al. 2014; Price et al. 2016; Wuyts et al. 2016), which has also been postulated as the driver of the black-hole to stellar mass relation at high- z (Maiolino et al. 2024). This would mean, consequently, that low-mass galaxies at high redshift have higher gas fractions than their massive counterparts, a

fact that has been well-established in the $z \geq 1$ literature (Scoville et al. 2017; Liu et al. 2019; Dessauges-Zavadsky et al. 2020). It is worth noticing (see also de Graaff et al. 2024), however, that the magnitude of the discrepancy –an order of magnitude on average, but up to ≈ 2 dex in some cases– is significantly larger than previous lower redshifts studies at similarly low stellar masses (e.g., Maseda et al. 2013).

To test the aforementioned hypothesis, we look at the gas masses implied by the SFRs of our high- z samples. First, we investigate the correlation between the M_\star/M_{dyn} and Σ_{SFR} as a proxy of the gas-mass surface density in galaxies (Σ_{gas} , Kennicutt 1998). We found a tentative anti-correlation between M_\star/M_{dyn} and Σ_{SFR} where galaxies with higher Σ_{SFR} show lower M_\star/M_{dyn} ratios (lower panel of the Fig. 7). A similar correlation between M_\star/M_{dyn} and Σ_{SFR} was found by Wuyts et al. (2016), in a sample of massive galaxies at $0.6 \leq z \leq 2.6$. While the SFRs of high- z samples are lower than Cosmic Noon massive galaxies, their star formation is more concentrated (smaller r_e), henceforth increasing the Σ_{SFR} . In addition to their low M_\star/M_{dyn} ratios, this imply higher gas mass fractions in these high redshift systems, in agreement with predictions from cosmological simulations too (Pillepich et al. 2019).

Are the implied gas masses enough to reconcile baryonic and dynamical masses? In order to address this question, we use the combined $\Sigma_{\text{SFR}} - \Sigma_{\text{gas}}$ relation (including normal and starburst galaxies) in Kennicutt & De Los Reyes (2021) to give a rough estimate of the total gas mass surface density⁸. Ultimately, GO1871 galaxies show $\Sigma_{\text{SFR}}/M_\odot\text{yr}^{-1}\text{kpc}^{-2} = 0.3 - 20$, which translate into $\Sigma_{\text{gas}}/M_\odot\text{yr}^{-1}\text{kpc}^{-2} = 140 - 3300$. Accounting for galaxy sizes in the morphologically resolved sources, $r_e = 0.08 - 0.18$ arcsec (or 400 – 960 pc), we obtain gas masses of $\log M_{\text{gas}} \approx 8.2 - 9.5 M_\odot$, implying gas-to-stellar mass fractions of $f_{\text{gas}} \approx 0.65$, on average. These large f_{gas} are consistent with the large measured Σ_{SFR} values.

The potential total baryon contribution including the gas phase, $M_{\text{baryon}} = M_\star + M_{\text{gas}}$, only reconciles baryonic and dynamical masses in 2 out of the 11 (resolved) GO1871 galaxies. For the remaining cases, M_{dyn} is still larger than the total baryonic mass by an inverse factor of $M_{\text{baryon}}/M_{\text{dyn}} \approx 0.2 - 0.7$. A further increase of the gas masses at fixed Σ_{SFR} –i.e., an offset in the star-formation law relation– would require decreasing the star formation efficiency (SFE) in these high- z systems. This scenario, nevertheless, seems unlikely for two reasons. First, there is already an established scaling relation in the local Universe that predicts an increase (or flattening, but never a decrease) of the SFE with Σ_{SFR} (Leroy et al. 2008). In addition, such a significant decrease in SFE would go against the claim of a boost in SFE at high- z to explain the over abundance of UV-bright galaxies observed by *JWST* (e.g., Li et al. 2024; Dekel et al. 2023; Wang et al. 2023). Even under the assumption that these galaxies may host an over-massive BH, similar to the recently discovered Little Red Dots (Furtak et al. 2023; Kokorev et al. 2023; Larson et al. 2023; Übler et al. 2023; Lambrides et al. 2024) and other broad and narrow-line AGNs at high- z (e.g., Harikane et al. 2023; Chisholm et al. 2024; Maiolino et al. 2024), the maximum contribution of the BH to the baryonic mass would not exceed 0.1 dex, insufficient to account for the mass discrepancy. In any case, the absence of broad line regions in the spectra of GO1871

galaxies, and the lack of high-ionization lines (except for the IMBH candidate) makes this scenario unlikely.

All this said, there is still the possibility of M_{dyn} being overestimated. As widely discussed in de Graaff et al. (2024), the underlying assumptions in the M_{dyn} equation can only yield an over-estimation of the dynamical mass by 0.3 – 0.6 dex, at most. Likewise, the over-estimation of M_{dyn} due to the dominance of outflow components or turbulence due to stellar feedback in the line profiles is unlikely and negligible, respectively (see also discussion in Übler et al. 2019). Neither we can discard systematic underestimations of stellar mass, due to (1) SFH assumptions (e.g., Maraston et al. 2010; Whitler et al. 2023) and (2) the lack of ability of the NIRCcam photometry to capture the light from an older (redder) stellar population. This older stellar population may dominate the mass budget but the younger stellar population is out-shining the older stellar population (e.g., Papovich et al. 2001; Narayanan et al. 2024). Unfortunately, current data do not allow us to draw further conclusions in this direction.

5 GAS FLOWS BEYOND COSMIC NOON

Before the launch of *JWST*, the properties of gaseous winds beyond Cosmic Noon galaxies remained uncharted territory, relegated to a few number of studies from the ground. These studies targeted the ionized gas traced by rest-UV transitions (e.g., Sugahara et al. 2019), or the sub-mm regime with ALMA, probing both the cold molecular (e.g., Jones et al. 2019; Spilker et al. 2020) and warm ionized phases (e.g., Gallerani et al. 2018; Ginolfi et al. 2020; Akins et al. 2022). By exploiting the capabilities of NIRSspec, we now study the properties of warm ionized gas-flows in our sample of $z = 4 - 8$ galaxies.

The presence of ionized gas-flows in GO1871 spectra is based on the statistical preference of a two-component versus a single Gaussian fit to the [O III] λ 5008 line profile. Following the methods outlined in Sect. 2, we detect five gas-flow candidates out of 16 galaxies with [O III] observations. This translates into a 30 per cent detection rate. Although this is in agreement with other NIRSspec studies at similar redshifts, it is still slightly higher than Xu et al. (2023, who use lower resolution gratings and therefore might be incomplete) but lower than Carniani et al. (2024, probably due to their larger sample size). GO1871 gas-flow candidates have $\log M_\star/M_\odot = 7.75 - 9.25$ and $\text{SFR}_{10}/M_\odot\text{yr}^{-1} \approx 10$ at redshifts of $z = 6.5 - 7.5$ (i.e, deep into the EoR). The gas-flow candidates have high Σ_{SFR} values of $\Sigma_{\text{SFR}}/M_\odot\text{yr}^{-1}\text{kpc}^{-2} \approx 1$, and show evidence of recent bursts in the SFH, as suggested by their high burstiness parameters ($\text{SFR}_{10}/\text{SFR}_{100} \geq 1$). The gas-flow galaxies have stellar masses below the median of the full GO1871 sample, while their SFR, Σ_{SFR} , and burstiness parameter are high compared to the GO1871 galaxies that do not show gas-flow signatures.

The flux ratio between the gas-flow (*broad*) and the static components (*narrow*) lays in the range $F_B/F_N = 0.17 - 0.98$. These values are typical of star-forming galaxies in the nearby Universe (see the recent Arribas et al. 2014; Reichardt Chu et al. 2022; X. Xu et al. 2024). A positive correlation between F_B/F_N and stellar mass, extending below $10^8 M_\odot$, has been suggested by some authors (e.g., Newman et al. 2012; Freeman et al. 2019; X. Xu et al. 2024), as the results of the stronger outflows powered by more massive galaxies. Some other works, however, do not find such trend (Swinbank et al. 2019; Perrotta et al. 2021; Concas et al. 2022). Interestingly, three out of five galaxies show an asymmetry in the [O III] line profile where the red wing is more prominent than the blue wing. In other words, their gas-flow component is redshifted with respect to the

⁸ The following gas masses should be taken with caution, as the Kennicutt & De Los Reyes (2021) relation has been calibrated in the local Universe and assumes a constant star-formation efficiency, which may not apply to high- z galaxies (see Tacconi et al. 2020)

static component, with a velocity offset $\Delta v = v_{\text{narrow}} - v_{\text{broad}} < 0$, beyond the 3σ significance in all cases. This result is in contrast to the well-established picture of ionized outflows in the local Universe (see [Thompson & Heckman 2024](#), for a review), where blue-wing asymmetries are almost ubiquitous and attributed to gas-flows, since neither rotation nor mergers can account for such observed profile (i.e., they would not make the second component systematically broad and blue-shifted, see [Harrison et al. 2014](#)). This being said, the presence of redshifted gas-flow components is not unseen (e.g., [Ruschel-Dutra et al. 2021](#)). Authors usually assume that the broad component primarily traces outflowing material, and the shift (blue or red) depends on the geometry and on the line of sight (see discussion in [Llerena et al. 2023](#)). In the remaining of this section, we will follow this interpretation. Based on the low dust content of our galaxies, in Section 5.3 we will explore whether these flows can be explained as inflows on the near-side of the galaxy. However we are not able to definitively determine whether the flows are inflowing, and we conclude that outflows are the most likely origin of these flows. We will sometimes refer to both inflow and outflow candidates as *gas flows* due to this uncertainty.

Following commonly used techniques in the literature, we now proceed to characterize the physical properties of the outflow (see appendix's Table A3), namely the maximal outflow velocity (or v_{flow}), mass outflow rate (\dot{M}_{flow}) and mass loading factor (η). We also perform a thorough literature comparison, by putting together the following data sets (sorted by redshift):

- [Marasco et al. \(2023\)](#): sample of 19 nearby ($z \simeq 0$) star-forming galaxies with available optical VLT/MUSE spectroscopy. See the paper for references.
- [Llerena et al. \(2023\)](#): selection of 35 star-forming galaxies at $z \simeq 3$ from the VUDS ([Le Fèvre et al. 2015](#)) and VANDELs ([Garilli et al. 2021](#)) surveys, with ground-based NIR spectroscopy from Keck/MOSFIRE ([Kriek et al. 2015](#); [Cullen et al. 2021](#)) and VLT/XShooter ([Amorín et al. 2017](#)).
- [Carniani et al. \(2024\)](#): high-resolution observations of 52 galaxies with NIRSpc G395H/F270LP at $z = 4 - 7$, as part of the JADES survey ([Eisenstein et al. 2023](#)).
- [Xu et al. \(2023\)](#): compilation of 130 *JWST* NIRSpc and NIR-Cam WFSS spectra at $z = 3 - 9$, taken from various *JWST* programs (ERO, CEERS, FRESCO, GLASS, and JADES). See the paper for references.

These samples have been carefully chosen to cover similar stellar mass ranges ($\log M_{\star}/M_{\odot} = 7 - 10$) but different look-back times (from local galaxies and Cosmic Noon, and beyond). Still, they have very distinct SFRs: local dwarfs have low SFR overall ([Marasco et al. 2023](#), $\text{SFR}_{10}/M_{\odot}\text{yr}^{-1} = 0.1 - 1$), while highly star-forming galaxies at Cosmic Noon have elevated SFRs ([Llerena et al. 2023](#), $\text{SFR}_{10}/M_{\odot}\text{yr}^{-1} = 10 - 100$). The high-redshift samples ([Xu et al. 2023](#); [Carniani et al. 2024](#)) show intermediate $\text{SFR}_{10}/M_{\odot}\text{yr}^{-1} = 1 - 10$.

5.1 Outflow scaling relations

Without further ado, we first compute the maximum velocity of the outflow (v_{flow} , [Rupke et al. 2005](#)) as

$$v_{\text{flow}} = |v_{\text{broad}} - v_{\text{narrow}}| + \sigma_{\text{broad}}, \quad (6)$$

where σ_{broad} is the velocity dispersion of the broad component of the [O III] line, and $v_i = c \cdot (\lambda_{i,0} - \lambda_{\text{rest}}) / \lambda_{\text{rest}}$ corresponds to the velocity shift (in km s^{-1}) between the narrow (static) and broad (outflow) components. The upper panel of Figure 8 shows v_{flow} versus M_{\star}

and SFR for our GO1871 gas-flow candidates, where red-shifted components have been denoted with '+' and normal blue-shifted ones with empty symbols. GO1871 outflows show moderate v_{flow} in the range $150 - 250 \text{ km s}^{-1}$, compatible with other samples at high redshift (e.g., [Xu et al. 2023](#)). The combination of all samples show a weak $v_{\text{flow}} - M_{\star}$ correlation with large scatter, only marginally consistent with the numerical prediction of an increasing v_{flow} with stellar mass (e.g., [Nelson et al. 2019](#)). The SFR averaged over the last 10 Myr (SFR_{10}) seems to be a more direct proxy of the speed of the outflow, where v_{flow} increasing with increasing SFR_{10} is more evident among the individual galaxy samples.

Next, we compute the mass of ionized gas that is being expelled by the outflow. Assuming photo-ionization ([Carniani et al. 2015](#)), the gas mass of the ionized outflow (M_{flow}) can be estimated from the luminosity of the [O III] broad component ($L_{[\text{O III}]}$) and the metallicity of the outflow as in,

$$M_{\text{flow}} (M_{\odot}) = 0.6 \times 10^8 \left(\frac{L_{[\text{O III}]}}{10^{44} \text{ erg/s}} \right) \left(\frac{Z_{\text{flow}}}{Z_{\odot}} \right)^{-1} \left(\frac{n_{\text{flow}}}{350 \text{ cm}^{-3}} \right)^{-1}, \quad (7)$$

where we assume $Z_{\text{flow}}/Z_{\odot} = 0.1$ for the metallicity and $n_{\text{flow}}/350 \text{ cm}^{-3} = 1$ for the electron number density of the outflow. Ionized gas abundances of 10 per cent the solar value are consistent with the R_{23} ratios measured in GO1871 galaxies (see Fig. 4), and it is also typical of high- z galaxies at these stellar masses (see e.g., [Nakajima et al. 2023](#); [Curti et al. 2024](#); [Sanders et al. 2024](#), using the direct T_e method). Likewise, the chosen input value for the outflow density (e.g., [Isobe et al. 2023](#); [Reddy et al. 2023](#)) is based on independent measurements of the electron number density (n_e) using the [O II] $\lambda\lambda 3727, 29$ doublet ([Stephenson et al.](#), in preparation).

Then, the mass outflow rate (\dot{M}_{flow}) is defined as the amount of gas expelled due to the galactic wind per unit time. Assuming a spherical geometry, a unity covering fraction, and a constant \dot{M}_{flow} with time ([Lutz et al. 2020](#)), this quantity can be computed as:

$$\dot{M}_{\text{flow}} = M_{\text{flow}} \frac{v_{\text{flow}}}{r_{\text{flow}}}, \quad (8)$$

where v_{flow} and M_{flow} are the maximal velocity of the outflow and the outflow mass calculated above. r_{flow} characterizes the extension of the outflow, and it is assumed to be twice the effective radius ($2r_e$, i.e., the radius that encompasses *all* the galaxy light) measured in the NIRCcam mosaics. The resulting mass outflow rates for GO1871 and literature samples are presented in the lower panel of Fig. 8 as a function of stellar mass and SFR_{10} . The dynamical range of the \dot{M}_{flow} is large, with outflow rates in the nearby dwarfs of [Marasco et al. \(2023\)](#) falling four orders of magnitude apart from the sample of highly star-forming galaxies of [Llerena et al. \(2023\)](#) at the peak of cosmic star-formation (see also [Förster Schreiber et al. 2019](#)). High- z samples lay in between these two regimes, with moderate $\dot{M}_{\text{flow}}/M_{\odot}\text{yr}^{-1} = 0.2 - 5$ (e.g., [Carniani et al. 2024](#)).

At fixed M_{\star} , literature \dot{M}_{flow} measurements at different cosmic epochs span a wide range. An underlying \dot{M}_{flow} correlation becomes more clear with SFR. Moving from low to high SFR_{10} , mass outflow rates monotonically increase, with a slope that qualitatively matches the predictions from mock winds ($\dot{M}_{\text{flow}} \propto \text{SFR}^{0.7}$) in cosmological simulations including realistic feedback recipes (FIRE-like simulation, see [Hopkins et al. 2012](#)). Measurements of \dot{M}_{flow} in high- z galaxies such as this work, [Xu et al. \(2023\)](#) or [Carniani et al. \(2024\)](#), bridge the gap in the outflow landscape by probing moderate SFR and \dot{M}_{flow} .

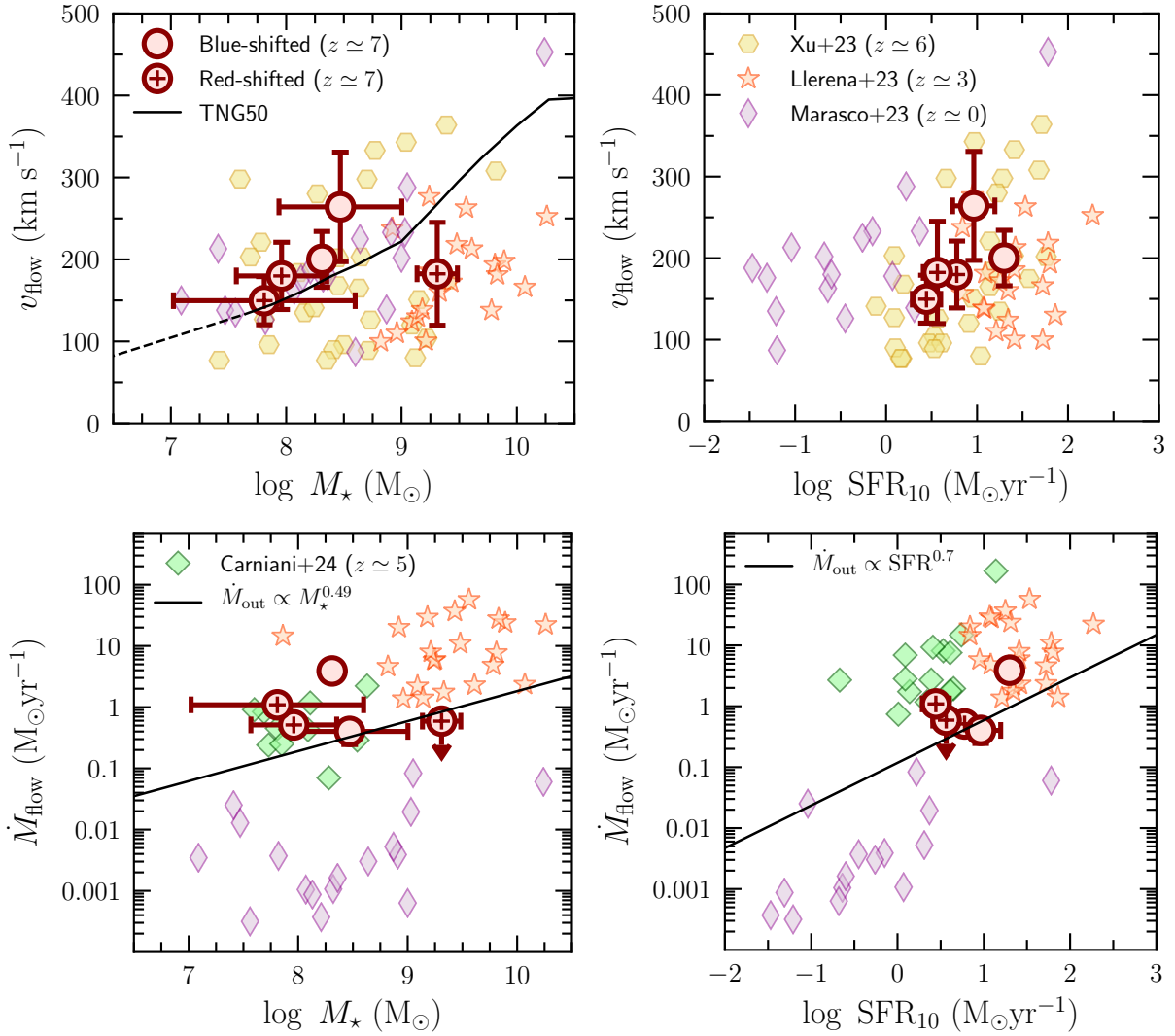


Figure 8. Maximum gas-flow velocity (v_{flow}) and mass flow rate (\dot{M}_{flow}) as a function of galaxy stellar mass (M_{\star}) and SFR_{10} . Thick circles show our high- z gas-flows candidates (galaxies showing red-shifted components are marked with a '+', the rest show blue-shifted components). Literature measurements at $z \approx 6$ (Xu et al. 2023), $z \approx 5$ (Carniani et al. 2024), $z \approx 3$ (Llerena et al. 2023) and $z \approx 0$ (Marasco et al. 2023) are displayed via hexagons, thick diamonds, stars and thin diamonds, respectively. Black lines highlight the predictions from TNG50 cosmological simulations (*top-left*: Nelson et al. 2019) and FIRE-like cosmological simulations (*bottom*: Hopkins et al. 2012).

Both moderate outflow velocities (a few hundreds km s^{-1}) and mass outflow rates comparable to the SFR are standard among starburst-driven winds in typical L^{\star} galaxies in the local Universe (e.g., see review article by Veilleux et al. 2020). Correlations between v_{flow} , \dot{M}_{flow} , M_{\star} and SFR are expected for this type of winds (e.g., Murray et al. 2005; Rupke et al. 2005; Heckman et al. 2015). On the one hand, faster outflows (high v_{flow}) are usually associated with higher SFRs (Arribas et al. 2014; Chisholm et al. 2015): more vigorous star formation events would inject greater amounts of energy and momentum into the ISM, driving more powerful winds. Similarly, \dot{M}_{flow} scales exponentially with SFR (Xu et al. 2022b; Marasco et al. 2023), since the star-formation-driven feedback is proportional to the stellar production rate. On the other hand, the scaling with M_{\star} arises from the interplay between feedback energy and gravitational binding energy, introducing more scatter into the scaling relations with stellar mass.

The efficiency of galactic outflows to regulate star formation is

parameterized by the mass loading factor, η (Heckman et al. 1990), measuring the amount of ejected gas relative to the rate at which the galaxy forms stars. In other words, η can be defined as the ratio of the mass outflow rate to the galaxy SFR (e.g., Veilleux et al. 2005),

$$\eta = \frac{\dot{M}_{\text{flow}}}{\text{SFR}}, \quad (9)$$

where for SFR we use SFR_{10} . $\eta \geq 1$ can lead to gas depletion in the galaxy, reducing the potential for future star formation, although the presence of gas in hotter phases, and the mass transfer between them makes this interpretation rather simplistic (e.g., Fielding & Bryan 2022).

Figure 9 shows the mass loading factor for both our GO1871 ($\eta \approx 0.04 - 0.4$) and literature samples, as a function of the galaxy stellar mass. Low-mass galaxies at high redshift (Xu et al. 2023, and this work) show mass loading factors below unity. Again, observed mass loadings span three order of magnitudes, with some local dwarfs having the least efficient winds. Cosmic Noon (Ller-

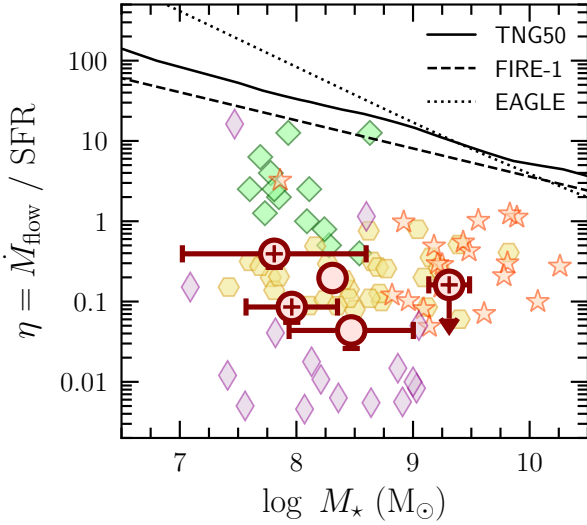


Figure 9. Mass loading factor (η) versus galaxy stellar mass (M_\star). The solid, dashed and dotted lines show the median for different cosmological simulations: TNG50 (Nelson et al. 2019) and EAGLE (Mitchell et al. 2020), both at $z = 2$, and FIRE-1 (regardless of the redshift, Muratov et al. 2015), respectively. Symbols are the same as in Fig. 8. At fixed M_\star , outflows in high- z galaxies are *more efficient* at removing gas from the star forming regions than in the local Universe.

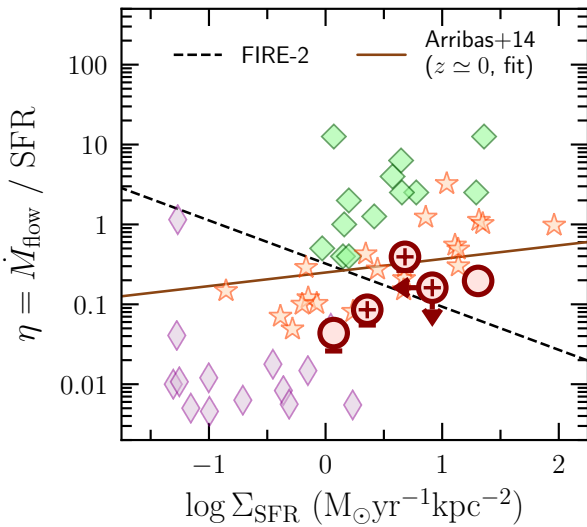


Figure 10. The relation between the mass loading factor (η) and the SFR surface density (Σ_{SFR}). The red-solid and dashed lines correspond to the linear fits performed over the local observations from Arribas et al. (2014), and to mock galaxies in the FIRE-2 simulations Pandya et al. (2021). Symbols are the same as in Fig. 8. Galaxies that host a more compact star formation activity show more efficient outflows.

ena et al. 2023) and star-forming systems at higher redshifts show similar mass loadings, with the exception of Carniani et al. (2024), exceeding beyond $\eta \geq 1$. In conclusion, at fixed M_\star or SFR, outflows in high- z galaxies are *more efficient* in removing baryons than galaxies in the local Universe, in contrast with some of the proposed *feedback-free* scenarios to explain the abundance of early galaxies (e.g., Li et al. 2024; Dekel et al. 2023; Wang et al. 2023). As we will argue in the next section, and thanks to their low dynamical

masses, outflows in high- z galaxies may have the ability to escape the gravitational potential of the host and enrich the CGM.

According to theoretical expectations (Murray et al. 2005) and numerical simulations (Muratov et al. 2015), the mass loading factor of star-formation driven winds should decrease with increasing stellar mass, almost independently of redshift (Nelson et al. 2019). This means that the feedback in low-mass galaxies is more effective at expelling gas compared to more massive galaxies, where outflows may be suppressed by stronger gravitational potentials. The slope derived from simulations, $\eta \propto M_\star^{-0.3}$, is consistent with some works (e.g., Chisholm et al. 2017; Förster Schreiber et al. 2019; Stanton et al. 2024), although this conclusion becomes scarce once the different galaxy samples are looked at separately (see also McQuinn et al. 2019). Perhaps more surprising is the fact that, compared to the compilation of measurements in Fig. 9, cosmological simulations overshoot the normalization in the $\eta - M_\star$ relation, e.g., by more than a factor of $\times 10$ in the latest, state-of-the-art FIRE-2 simulation (Pandya et al. 2021). This may indicate that there is a significant fraction of outflow mass in the hot phase, that the rest-optical nebular lines are unable to probe. At masses higher than $\log M_\star / M_\odot \geq 10$, a possible turnover of the mass loading has been associated with AGN-driven winds by some observational (Swinbank et al. 2019; Concas et al. 2022) and numerical works (Mitchell et al. 2020), although this topic is constantly under revision (see the recent Weldon et al. 2024).

Finally, our gas-flow candidates also show some of the lowest M_\star / M_{dyn} but highest Σ_{SFR} within the GO1871 sample, with evidence of recent burst of star-formation in their SED via $\text{SFR}_{10} / \text{SFR}_{100} \geq 1$, and whose intensity also scales with Σ_{SFR} (Fig. 3). This reveals a picture in which high gas densities are needed in order to foster intense and compact star-forming events, that will eventually lead to the launch of star-formation driven outflows (e.g., Heckman 2002). In Figure 10, we investigate the relationship between the estimated mass loading factor and the compactness of the star formation (Σ_{SFR}) for our high- z galaxies and comparison samples at lower redshifts. Observationally, a positive, significant correlation exist between η and Σ_{SFR} (see e.g., the linear fit by Arribas et al. 2014). Consistently, intense outflows have been observed ubiquitously among high Σ_{SFR} galaxies in other samples, showing faster velocities, higher mass outflow rates and increasing mass loading factors with Σ_{SFR} (e.g., Newman et al. 2012; Arribas et al. 2014; Davies et al. 2019; Reichardt Chu et al. 2022; Llerena et al. 2023). In contrast, hydrodynamical simulations predict a negative trend between η and Σ_{SFR} , like due to the inverse proportionality of the $\eta - \Sigma_{\text{gas}}$ relation (e.g., Hopkins et al. 2012; Pandya et al. 2021).

5.2 Outflows enrich the CGM at high- z

An important question to address is whether the outflows detected in our sample of high- z galaxies would remain bound to the gravitational influence of the host galaxy. In the case of metal-enriched outflows (e.g., Chisholm et al. 2018; Hamel-Bravo et al. 2024), this will determine the ability of the gas to escape and reach the CGM (e.g., Muratov et al. 2017). To approach this question, we compare the outflow velocity to the escape velocity given by the dynamical mass of the host galaxy. An approximation to the mean escape velocity (v_{esc}), measured at a distance r_0 , is given in Arribas et al. (2014),

$$v_{\text{esc}} \approx \left(\frac{2M_{\text{dyn}}G \times (1 + r_{\text{max}}/r_0)}{3r_0} \right), \quad (10)$$

assuming an isothermal gravitational potential that extends to a

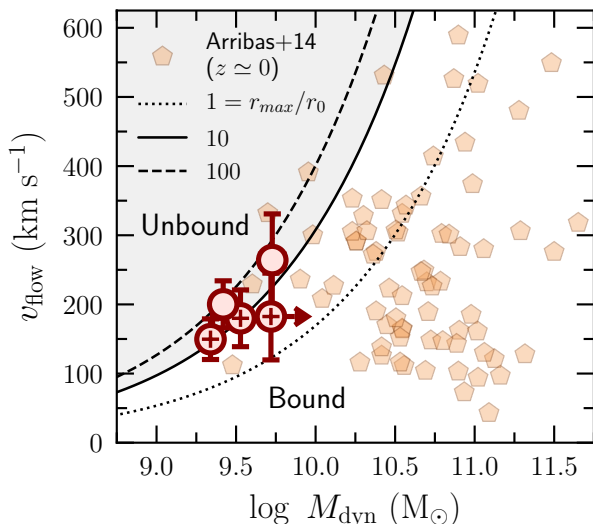


Figure 11. Relation between the gas-flow velocity (v_{flow}) and the dynamical mass (M_{dyn}). The local measurements by Arribas et al. (2014) are plotted with pentagons. The dotted, solid and dashed lines show the theoretical escape velocity (v_{esc}) at $r_0 = 3$ kpc, as a function of the dynamical mass for gravitational potentials extending out to $r_{\text{max}}/r_0 = 1, 10$ (default) and 100. Due to their low dynamical masses, galactic winds in low-mass galaxies at high- z will likely escape the gravitational potential of the host galaxy (*unbound* region), enriching the surrounding CGM.

maximum radius r_{max} (Heckman et al. 2000; Bellocchi et al. 2013). Figure 11 shows our GO1871 measurements of v_{flow} versus M_{dyn} , together with the local comparison sample of Arribas et al. (2014), at higher M_{dyn} 's. The dotted, solid and dashed lines correspond to $r_{\text{max}}/r_0 = 1, 10$ and 100 of the v_{esc} approximation, where the outflow velocity is measured at $r_0 = 3$ kpc (twice the median effective radius in our sample, approximately). We take the $r_{\text{max}}/r_0 = 10$ curve as reference (see e.g., Flury et al. 2023). As a result, points falling above the solid line in Fig. 11 will have outflow velocities higher than the escape velocity (*unbound* region). While the blue-shifted outflow candidates in our sample fulfill this condition, those identified as red-shifted gas-flow candidates are consistent with below the curve (although still within 1σ). In the former case, part of the ejected gas could escape the gravitational potential of the host galaxy and contribute to enriching the CGM with metals (e.g., Tumlinson et al. 2017; Guo et al. 2020), in line with the conclusions outlined in Carniani et al. (2024).

Last but not least, we highlight how the bulk of the Arribas et al. sample, composed of local luminous galaxies at $\log M_{\text{dyn}}/M_{\odot} \geq 10$, will most likely retain all their gas reservoirs: outflows will eventually cool down and fall back into the galaxy well in the form of galactic fountains. Xu et al. (2023) made a similar claim at high- z that their reported velocities were not high enough for the outflow to escape from the galactic potentials, despite probing almost identical values of M_{\star} , SFR, v_{flow} and \dot{M}_{flow} as in this work. Without measurement of M_{dyn} , Xu et al. relied on additional assumptions for the escape velocity (i.e., they were computed from the theoretical circular velocity of the dark-matter halo), this may be the origin of the discrepancy. To sum up, our observation of outflows in low-mass, high- z galaxies –with moderate velocities and mass loading factors– imply that stellar feedback is important for driving the baryon cycle at $z > 5$.

5.3 Tentative evidence of inflows in high- z galaxies

As mentioned above, three out of our five gas-flow candidates show red-shifted broad emission features in the [O III] profiles (Fig. 2), with no blue-shifted components detected. In the literature, this is usually attributed to outflows in the far-side of the line of sight (Arribas et al. 2014; Llerena et al. 2023), and throughout the previous section we have also adopted this interpretation. However, given the negligible dust attenuation measured in these galaxies (Sect. ??), one should expect to observe the blue-shifted counterpart of the expanding gas in the spectra as well (e.g., Ruschel-Dutra et al. 2021). Instead, and invoking analogous geometrical arguments, it is worth considering the prospect that the red-shifted broad emission line traces inflows of ionized gas from the near-side of the galaxy. If true, the high detection rate of inflows in high- z galaxies lays in contrast with observations of the nearby Universe, where the incidence of inflows is very low ($\leq 5\%$, from Rubin et al. 2014). This behavior is expected, as the specific gas accretion rate on to dark matter haloes decreases with decreasing redshift (e.g., van de Voort et al. 2011), but it has not been tested observationally to date.

The evidence of galactic inflows in our high- z galaxies is supported by additional factors. For instance, the maximum velocity (Fig. 8) of the red-shifted components ($v_{\text{flow}} \leq 200 \text{ km s}^{-1}$) is lower than for the outflow candidates ($v_{\text{flow}} \geq 200 \text{ km s}^{-1}$), as expected for inflows (e.g., Weldon et al. 2023). Indeed, the inferred escape velocity from the dynamical mass of the redshifted gas flows (Fig. 11) is *comparable* to the maximum velocity of the inflowing gas, and marginally consistent with them being gravitationally bound to the host galaxy and accreting at roughly the virial velocity of the halo (e.g., Goerdt & Ceverino 2015). Although an increase in velocity and mass inflow rate with M_{\star} and SFR is still expected, the v_{flow} and \dot{M}_{flow} scaling relation with galaxy properties will be different than those for the outflows (e.g., Martin et al. 2012; Roberts-Borsani et al. 2020). Unfortunately, our limited sample size prevent us to draw further conclusions.

Further, the mass loading factors are all below unity, which would indicate that the inflows are not sufficient to continue feeding the star-formation of the galaxy (e.g., Sánchez Almeida et al. 2014a). This hints that these galaxies will have a bursty SFH (e.g., Muratov et al. 2015), which is supported by the high burstiness parameters inferred from the SED, $\text{SFR}_{10}/\text{SFR}_{100} \geq 1$. Finally, the high Σ_{SFR} in these galaxies, and therefore the higher implied Σ_{gas} , likely requires a high gas accretion rate and likely leads to chemical inhomogeneities (e.g., Sánchez Almeida et al. 2014b; Cameron et al. 2021; del Valle-Espinosa et al. 2023). In other words, gas accretion from the cosmic web can fuel the star-formation (boosting Σ_{SFR}), increasing the gas fractions that would inevitably decrease the M_{\star}/M_{dyn} ratios seen in these high- z galaxies (Fig. 7). While tantalizing and a possible departure from local galaxies, the outflow scenario cannot be ruled out with the current data. Definitively testing the inflow hypothesis requires further observations (e.g., absorption lines, see Rubin et al. 2012). Consistently, we have adopted the outflows emerging from the far-side of the ISM as the main physical picture of the gas flows detected in this paper.

6 CONCLUSIONS

In this paper, we explore the ionized gas kinematics, dynamical mass and gas-flow properties of high- z galaxies. To do so, we make use of high-resolution *JWST*/NIRSpec spectroscopy in the G235H/F170LP and G395H/F290LP gratings (Jakobsen et al.

2022). Our sample is composed of 16 moderately faint ($M_{\text{UV}} \approx -20$) star-forming galaxies at redshifts $4 \leq z \leq 7.6$ from program ID GO1871 (PI: Chisholm), ranging in log stellar masses of $\log M_{\star}/M_{\odot} = 7.75 - 9.75$, $\text{SFR}_{\text{H}\beta}/M_{\odot}\text{yr}^{-1} = 0.3 - 30$ and $\Sigma_{\text{SFR}}/M_{\odot}\text{yr}^{-1}\text{kpc}^{-2} = 0.3 - 20$. We summarize our main conclusions below.

- The nebular line ratios reveal a metal-poor, dustless and highly ionized ISM, with $\log O_{32} = 0.5 - 2$ and $\log R_{23} = 0.5 - 1.5$ comparable to other star-forming samples at high- z (e.g., Cameron et al. 2023; Mascia et al. 2023; Sanders et al. 2023), as well as to EELGs in the nearby Universe (e.g., Yang et al. 2017; Izotov et al. 2020; Flury et al. 2022).

- The width of the emission lines such as H β and [O III] is spectroscopically resolved. Accounting for instrumental broadening, the velocity dispersion of the ionized gas measured in our high- z sample is σ_{gas} (km/s) = 38 – 96. Including additional NIRSpect observations from de Graaff et al. (2024), we determine a mean σ_{gas} (km/s) = 56^{+16}_{-8} , comparable to more massive galaxies at lower redshifts (e.g., Förster Schreiber et al. 2018). We argue that the expected decrease in velocity dispersion due to the low stellar mass in these high- z systems (e.g., Pillepich et al. 2019), is driven by the increased turbulence at high redshift (e.g., Übler et al. 2019).

- Together with the galaxy sizes ($r_e = 400 - 960$ pc) modeled from archival NIRCcam imaging (Oesch et al. 2023), the resolved [O III] lines allow us to estimate the dynamical mass. Following Maiolino et al. (2024), we obtain $\log M_{\text{dyn}}/M_{\odot} = 9.25 - 10.25$, which leads to surprisingly low stellar-to-dynamical mass ratios in these high- z galaxies, i.e., $\log M_{\star}/M_{\text{dyn}} \in [-0.5, -2]$.

- The M_{\star}/M_{dyn} ratio shows a tentative, decreasing correlation with increasing Σ_{SFR} , suggesting higher gas-mass densities and gas fractions (average $f_{\text{gas}} = 0.65$) with increasing M_{\star}/M_{dyn} ratio. As widely discussed in de Graaff et al. (2024), the contribution of the inferred gas masses to the total baryonic mass does not solve the mass discrepancy. To reconcile the mass ratios, $M_{\text{baryon}}/M_{\text{dyn}} = (M_{\star} + M_{\text{gas}})/M_{\text{dyn}} \approx 0.2 - 0.7$, would require invoking other mechanisms such as a significant decrease of the star-formation efficiency, as opposed to recently proposed scenarios to explain the over-abundance of UV-bright galaxies at high-redshift with JWST (e.g., Wang et al. 2023).

- Evidence of gas-flows is found in five out of 16 galaxies (≈ 30 per cent incidence rate) based upon the statistical need of broad components to reproduce the wings of the [O III] lines. We compute the properties of the gas flow, namely outflow velocities (v_{flow} (km/s) = 150 – 250) and mass outflow rates ($\dot{M}_{\text{flow}}/M_{\odot}\text{yr}^{-1} = 0.2 - 5$), reporting values comparable to Xu et al. (2023) at similarly high redshifts.

- In the context of starburst-driven outflows, low-mass, high- z galaxies bridge the gap in the outflow scaling relations between the dwarf regime in the nearby Universe (Marasco et al. 2023), and more massive, highly star-forming galaxies at Cosmic Noon (Llerena et al. 2023), showing moderate v_{flow} and \dot{M}_{flow} , and mass loading factors $\eta = 0.04 - 0.4$. As a result, warm ionized outflows in high- z galaxies are *more efficient* in removing baryons from star-forming regions than galaxies in the local Universe with the same stellar mass.

- Our high- z outflow candidates are also among the lowest M_{\star}/M_{dyn} and highest Σ_{SFR} in the sample, showing that more recent bursts of star-formation ($\text{SFR}_{10}/\text{SFR}_{100} \geq 1$) have elevated star formation rate surface densities (Σ_{SFR}). These findings emphasize the need for both high gas-mass surface densities (high Σ_{SFR}) and bursty SFHs to foster intense, compact star-formation events

that launch galactic winds (e.g., Heckman 2002; Reichardt Chu et al. 2022).

- We compare the outflow velocity to the escape velocity given by the dynamical mass of the galaxy (following Arribas et al. 2014), and find that these high- z ionized outflows will likely escape the gravitational influence of the host, potentially enriching the CGM with metals (see also Carniani et al. 2024).

- Three out of the five gas-flow candidates show tentative signatures of inflows, with broad, red-shifted components in the [O III] line profile. In this cases, the maximum velocity of the inflow is lower than the outflow velocity in the other candidates, and below the escape velocity that is estimated from the dynamical mass. If confirmed, our findings would imply a much higher incidence of inflows compared to the nearby Universe (e.g., Martin et al. 2012; Rubin et al. 2014). The accretion of gas would also increase the gas fractions, in agreement with the high Σ_{SFR} , low M_{\star}/M_{dyn} ratios, and bursty SFHs in these high- z systems.

This work highlights the importance of high-resolution spectroscopic surveys with NIRSpect to study the baryon cycle of galaxies beyond Cosmic Noon. Providing one of the first evidences of stellar feedback and baryonic budget during the Epoch of Reionization, our results imply that inflows and outflows are important for driving the baryon cycle at early epochs of galaxy formation.

ACKNOWLEDGEMENTS

The authors thank M. G. del Valle-Espinosa and T. M. Stanton for helping with figure formatting. ASL acknowledges support from Knut and Alice Wallenberg Foundation. MJH is supported by the Swedish Research Council (Vetenskapsrådet) and is Fellow of the Knut and Alice Wallenberg Foundation. NGG and YII acknowledge support from the National Academy of Sciences of Ukraine by its project no.0123U102248 and from the Simons Foundation. This work is based (in part) on observations made with the NASA/ESA/CSA James Webb Space Telescope. The data were obtained from the Mikulski Archive for Space Telescopes at the Space Telescope Science Institute, which is operated by the Association of Universities for Research in Astronomy, Inc., under NASA contract NAS 5-03127 for JWST. These observations are associated with program #01871.

DATA AVAILABILITY

Any additional product and/or data underlying this article will be shared on reasonable request to the corresponding author.

REFERENCES

- Akins H. B., et al., 2022, *ApJ*, 934, 64
 Allen N., et al., 2024, *arXiv e-prints*, p. arXiv:2410.16354
 Amorín R., Pérez-Montero E., Vílchez J. M., Papaderos P., 2012a, *ApJ*, 749, 185
 Amorín R., Vílchez J. M., Hägele G. F., Firpo V., Pérez-Montero E., Papaderos P., 2012b, *ApJ*, 754, L22
 Amorín R., et al., 2017, *Nature Astronomy*, 1, 0052
 Amorín R. O., et al., 2024, *A&A*, 682, L25
 Arribas S., Colina L., Bellocchi E., Maiolino R., Villar-Martín M., 2014, *A&A*, 568, A14
 Atek H., et al., 2011, *ApJ*, 743, 121

- Atek H., Furtak L. J., Oesch P., van Dokkum P., Reddy N., Contini T., Illingworth G., Wilkins S., 2022, *MNRAS*, **511**, 4464
- Backhaus B. E., et al., 2024, *ApJ*, **962**, 195
- Barro G., et al., 2019, *ApJS*, **243**, 22
- Behroozi P. S., Wechsler R. H., Conroy C., 2013, *ApJ*, **770**, 57
- Belli S., Newman A. B., Ellis R. S., 2014, *ApJ*, **783**, 117
- Bellocchi E., Arribas S., Colina L., Miralles-Caballero D., 2013, *A&A*, **557**, A59
- Berg D. A., et al., 2022, *ApJS*, **261**, 31
- Bouwens R. J., et al., 2015, *ApJ*, **803**, 34
- Bouwens R. J., et al., 2021, *AJ*, **162**, 47
- Brammer G., 2023, msaexp: NIRSpc analysis tools, Zenodo, doi:10.5281/zenodo.7299500
- Brinchmann J., Pettini M., Charlot S., 2008, *MNRAS*, **385**, 769
- Bruzual G., Charlot S., 2003, *MNRAS*, **344**, 1000
- Calabrò A., et al., 2022, *A&A*, **667**, A117
- Calzetti D., Armus L., Bohlin R. C., Kinney A. L., Koornneef J., Storchi-Bergmann T., 2000, *ApJ*, **533**, 682
- Cameron A. J., et al., 2021, *ApJ*, **918**, L16
- Cameron A. J., et al., 2023, *A&A*, **677**, A115
- Cappellari M., et al., 2006, *MNRAS*, **366**, 1126
- Cardamone C., et al., 2009, *MNRAS*, **399**, 1191
- Carnall A. C., McLure R. J., Dunlop J. S., Davé R., 2018, *MNRAS*, **480**, 4379
- Carniani S., et al., 2015, *A&A*, **580**, A102
- Carniani S., et al., 2024, *A&A*, **685**, A99
- Chávez R., Terlevich R., Terlevich E., Bresolin F., Melnick J., Plionis M., Basilakos S., 2014, *MNRAS*, **442**, 3565
- Chisholm J., Tremonti C. A., Leitherer C., Chen Y., Wofford A., Lundgren B., 2015, *ApJ*, **811**, 149
- Chisholm J., Tremonti C. A., Leitherer C., Chen Y., 2017, *MNRAS*, **469**, 4831
- Chisholm J., Tremonti C., Leitherer C., 2018, *MNRAS*, **481**, 1690
- Chisholm J., Prochaska J. X., Schaerer D., Gazagnes S., Henry A., 2020, *MNRAS*, **498**, 2554
- Chisholm J., et al., 2024, *arXiv e-prints*, p. arXiv:2402.18643
- Concas A., et al., 2022, *MNRAS*, **513**, 2535
- Conroy C., Wechsler R. H., 2009, *ApJ*, **696**, 620
- Conselice C. J., et al., 2024, *MNRAS*, **531**, 4857
- Cullen F., et al., 2021, *MNRAS*, **505**, 903
- Curti M., Cresci G., Mannucci F., Marconi A., Maiolino R., Esposito S., 2017, *MNRAS*, **465**, 1384
- Curti M., Mannucci F., Cresci G., Maiolino R., 2020, *MNRAS*, **491**, 944
- Curti M., et al., 2024, *A&A*, **684**, A75
- Davies R. L., et al., 2019, *ApJ*, **873**, 122
- Dekel A., Silk J., 1986, *ApJ*, **303**, 39
- Dekel A., Sarkar K. C., Birnboim Y., Mandelker N., Li Z., 2023, *MNRAS*, **523**, 3201
- Dessauges-Zavadsky M., et al., 2020, *A&A*, **643**, A5
- Efstathiou G., 2000, *MNRAS*, **317**, 697
- Eisenstein D. J., et al., 2023, *arXiv e-prints*, p. arXiv:2306.02465
- Ejdetjärn T., Agertz O., Östlin G., Renaud F., Romeo A. B., 2022, *MNRAS*, **514**, 480
- Endsley R., et al., 2023, *arXiv e-prints*, p. arXiv:2306.05295
- Endsley R., et al., 2024, *MNRAS*, **533**, 1111
- Erb D. K., Steidel C. C., Shapley A. E., Pettini M., Reddy N. A., Adelberger K. L., 2006, *ApJ*, **646**, 107
- Erb D. K., Quider A. M., Henry A. L., Martin C. L., 2012, *ApJ*, **759**, 26
- Fabian A. C., 2012, *ARA&A*, **50**, 455
- Ferland G. J., et al., 2017, *Rev. Mex. Astron. Astrofis.*, **53**, 385
- Ferreira L., et al., 2022, *ApJ*, **938**, L2
- Ferreira L., et al., 2023, *ApJ*, **955**, 94
- Fielding D. B., Bryan G. L., 2022, *ApJ*, **924**, 82
- Finkelstein S. L., et al., 2013, *Nature*, **502**, 524
- Finkelstein S. L., et al., 2015, *ApJ*, **810**, 71
- Fiore F., et al., 2017, *A&A*, **601**, A143
- Flury S. R., et al., 2022, *ApJ*, **930**, 126
- Flury S. R., Moran E. C., Eleazer M., 2023, *MNRAS*, **525**, 4231
- Förster Schreiber N. M., Wuyts S., 2020, *ARA&A*, **58**, 661
- Förster Schreiber N. M., et al., 2018, *ApJS*, **238**, 21
- Förster Schreiber N. M., et al., 2019, *ApJ*, **875**, 21
- Fraternali F., Karim A., Magnelli B., Gómez-Guijarro C., Jiménez-Andrade E. F., Poses A. C., 2021, *A&A*, **647**, A194
- Freeman W. R., et al., 2019, *ApJ*, **873**, 102
- Fujimoto S., et al., 2022, *Nature*, **604**, 261
- Furtak L. J., et al., 2023, *ApJ*, **952**, 142
- Gallagher R., Maiolino R., Belfiore F., Drory N., Riffel R., Riffel R. A., 2019, *MNRAS*, **485**, 3409
- Gallerani S., Pallottini A., Feruglio C., Ferrara A., Maiolino R., Vallini L., Riechers D. A., Pavesi R., 2018, *MNRAS*, **473**, 1909
- Garilli B., et al., 2021, *A&A*, **647**, A150
- Gazagnes S., et al., 2024, *arXiv e-prints*, p. arXiv:2410.03337
- Genzel R., et al., 2014, *ApJ*, **796**, 7
- Genzel R., et al., 2017, *Nature*, **543**, 397
- Ginolfi M., et al., 2020, *A&A*, **633**, A90
- Goerdt T., Ceverino D., 2015, *MNRAS*, **450**, 3359
- González Delgado R. M., Leitherer C., Heckman T. M., 1999, *ApJS*, **125**, 489
- Green A. W., et al., 2010, *Nature*, **467**, 684
- Guo Y., et al., 2020, *ApJ*, **898**, 26
- Hamel-Bravo M. J., et al., 2024, *MNRAS*, **530**, 3855
- Harikane Y., et al., 2023, *ApJ*, **959**, 39
- Harrison C. M., Alexander D. M., Mullaney J. R., Swinbank A. M., 2014, *MNRAS*, **441**, 3306
- Hayward C. C., Hopkins P. F., 2017, *MNRAS*, **465**, 1682
- Heckman T. M., 2002, in *Mulchaey J. S., Stocke J. T., eds, Astronomical Society of the Pacific Conference Series Vol. 254, Extragalactic Gas at Low Redshift*. p. 292 (arXiv:astro-ph/0107438), doi:10.48550/arXiv.astro-ph/0107438
- Heckman T. M., Best P. N., 2014, *ARA&A*, **52**, 589
- Heckman T. M., Miley G. K., van Breugel W. J. M., Butcher H. R., 1981, *ApJ*, **247**, 403
- Heckman T. M., Armus L., Miley G. K., 1990, *ApJS*, **74**, 833
- Heckman T. M., Lehnert M. D., Strickland D. K., Armus L., 2000, *ApJS*, **129**, 493
- Heckman T. M., Alexandroff R. M., Borthakur S., Overzier R., Leitherer C., 2015, *ApJ*, **809**, 147
- Henry A., Berg D. A., Scarlata C., Verhamme A., Erb D., 2018, *ApJ*, **855**, 96
- Hernquist L., Springel V., 2003, *MNRAS*, **341**, 1253
- Hopkins P. F., Quataert E., Murray N., 2012, *MNRAS*, **421**, 3522
- Hutchison T. A., et al., 2019, *ApJ*, **879**, 70
- Isobe Y., Ouchi M., Nakajima K., Harikane Y., Ono Y., Xu Y., Zhang Y., Umeda H., 2023, *ApJ*, **956**, 139
- Izotov Y. I., Worseck G., Schaerer D., Guseva N. G., Thuan T. X., Fricke A. V., Orlitová I., 2018, *MNRAS*, **478**, 4851
- Izotov Y. I., Schaerer D., Worseck G., Verhamme A., Guseva N. G., Thuan T. X., Orlitová I., Fricke K. J., 2020, *MNRAS*, **491**, 468
- Izotov Y. I., Thuan T. X., Guseva N. G., 2021, *MNRAS*, **504**, 3996
- Izotov Y. I., Thuan T. X., Guseva N. G., 2024, *MNRAS*, **527**, 3486
- Jakobsen P., et al., 2022, *A&A*, **661**, A80
- Jaskot A. E., Oey M. S., 2013, *ApJ*, **766**, 91
- Johnson H. L., et al., 2018, *MNRAS*, **474**, 5076
- Jones G. C., Maiolino R., Caselli P., Carniani S., 2019, *A&A*, **632**, L7
- Jung I., et al., 2020, *ApJ*, **904**, 144
- Kassin S. A., et al., 2012, *ApJ*, **758**, 106
- Kennicutt R. C. J., 1998, *ARA&A*, **36**, 189
- Kennicutt R. C. J., De Los Reyes M. A. C., 2021, *ApJ*, **908**, 61
- Kennicutt R. C., Evans N. J., 2012, *ARA&A*, **50**, 531
- Kewley L. J., Dopita M. A., 2002, *ApJS*, **142**, 35
- Kobulnicky H. A., Kewley L. J., 2004, *ApJ*, **617**, 240
- Kohandel M., Pallottini A., Ferrara A., Zanella A., Rizzo F., Carniani S., 2024, *A&A*, **685**, A72
- Kokorev V., et al., 2022, *ApJS*, **263**, 38
- Kokorev V., et al., 2023, *ApJ*, **957**, L7

- Komarova L., Oey M. S., Krumholz M. R., Silich S., Kumari N., James B. L., 2021, *ApJ*, **920**, L46
- Kriek M., et al., 2015, *ApJS*, **218**, 15
- Kroupa P., 2001, *MNRAS*, **322**, 231
- Krumholz M. R., Thompson T. A., Ostriker E. C., Martin C. L., 2017, *MNRAS*, **471**, 4061
- Krumholz M. R., Burkhardt B., Forbes J. C., Crocker R. M., 2018, *MNRAS*, **477**, 2716
- Lambrides E., et al., 2024, *ApJ*, **961**, L25
- Larson R. L., et al., 2023, *ApJ*, **953**, L29
- Le Fèvre O., et al., 2015, *A&A*, **576**, A79
- Lehnert M. D., Nesvadba N. P. H., Le Tiran L., Di Matteo P., van Driel W., Douglas L. S., Chemin L., Bournaud F., 2009, *ApJ*, **699**, 1660
- Leroy A. K., Walter F., Brinks E., Bigiel F., de Blok W. J. G., Madore B., Thornley M. D., 2008, *AJ*, **136**, 2782
- Leung G. C. K., et al., 2019, *ApJ*, **886**, 11
- Li Z., Dekel A., Sarkar K. C., Aung H., Giavalisco M., Mandelker N., Tacchella S., 2024, *A&A*, **690**, A108
- Liu D., et al., 2019, *ApJ*, **887**, 235
- Llerena M., et al., 2023, *A&A*, **676**, A53
- Lutz D., et al., 2020, *A&A*, **633**, A134
- Lützgendorf N., et al., 2022, in Coyle L. E., Matsuura S., Perrin M. D., eds, Society of Photo-Optical Instrumentation Engineers (SPIE) Conference Series Vol. 12180, Space Telescopes and Instrumentation 2022: Optical, Infrared, and Millimeter Wave. p. 121800Y ([arXiv:2208.05355](https://arxiv.org/abs/2208.05355)), doi:10.1117/12.2630069
- Mai Y., et al., 2024, *MNRAS*, **533**, 3878
- Maiolino R., et al., 2008, *A&A*, **488**, 463
- Maiolino R., et al., 2024, *A&A*, **691**, A145
- Marasco A., et al., 2023, *A&A*, **670**, A92
- Maraston C., Pforr J., Renzini A., Daddi E., Dickinson M., Cimatti A., Tonini C., 2010, *MNRAS*, **407**, 830
- Martin C. L., 2005, *ApJ*, **621**, 227
- Martin C. L., Shapley A. E., Coil A. L., Kornei K. A., Bundy K., Weiner B. J., Noeske K. G., Schiminovich D., 2012, *ApJ*, **760**, 127
- Mascia S., et al., 2023, *A&A*, **672**, A155
- Maseda M. V., et al., 2013, *ApJ*, **778**, L22
- McClymont W., et al., 2024, *arXiv e-prints*, p. [arXiv:2405.15859](https://arxiv.org/abs/2405.15859)
- McElwain M. W., et al., 2023, *PASP*, **135**, 058001
- McQuinn K. B. W., van Zee L., Skillman E. D., 2019, *ApJ*, **886**, 74
- Mitchell P. D., Schaye J., Bower R. G., Crain R. A., 2020, *MNRAS*, **494**, 3971
- Muratov A. L., Kereš D., Faucher-Giguère C.-A., Hopkins P. F., Quataert E., Murray N., 2015, *MNRAS*, **454**, 2691
- Muratov A. L., et al., 2017, *MNRAS*, **468**, 4170
- Murray N., Quataert E., Thompson T. A., 2005, *ApJ*, **618**, 569
- Nakajima K., Ouchi M., 2014, *MNRAS*, **442**, 900
- Nakajima K., Ellis R. S., Iwata I., Inoue A. K., Kusakabe H., Ouchi M., Robertson B. E., 2016, *ApJ*, **831**, L9
- Nakajima K., Ellis R. S., Robertson B. E., Tang M., Stark D. P., 2020, *ApJ*, **889**, 161
- Nakajima K., Ouchi M., Isobe Y., Harikane Y., Zhang Y., Ono Y., Umeda H., Oguri M., 2023, *ApJS*, **269**, 33
- Narayanan D., et al., 2024, *ApJ*, **961**, 73
- Nelson D., et al., 2019, *MNRAS*, **490**, 3234
- Newman S. F., et al., 2012, *ApJ*, **761**, 43
- Newville M., Stensitzki T., Allen D. B., Rawlik M., Ingargiola A., Nelson A., 2016, Lmfit: Non-Linear Least-Square Minimization and Curve-Fitting for Python (ascl:1606.014)
- Oesch P. A., et al., 2023, *MNRAS*, **525**, 2864
- Oke J. B., Gunn J. E., 1983, *ApJ*, **266**, 713
- Onodera M., et al., 2016, *ApJ*, **822**, 42
- Onodera M., et al., 2020, *ApJ*, **904**, 180
- Pandya V., et al., 2021, *MNRAS*, **508**, 2979
- Papovich C., Dickinson M., Ferguson H. C., 2001, *ApJ*, **559**, 620
- Papovich C., et al., 2022, *ApJ*, **937**, 22
- Parlanti E., Carniani S., Pallottini A., Cignoni M., Cresci G., Kohandel M., Mannucci F., Marconi A., 2023, *A&A*, **673**, A153
- Pasha I., Miller T. B., 2023, *Journal of Open Source Software*, **8**, 5703
- Pelat D., Alloin D., 1980, *A&A*, **81**, 172
- Pelat D., Alloin D., Fosbury R. A. E., 1981, *MNRAS*, **195**, 787
- Perrotta S., et al., 2021, *ApJ*, **923**, 275
- Pillepich A., et al., 2019, *MNRAS*, **490**, 3196
- Popesso P., et al., 2023, *MNRAS*, **519**, 1526
- Price S. H., et al., 2016, *ApJ*, **819**, 80
- Price S. H., et al., 2020, *ApJ*, **894**, 91
- Prusinski N. Z., Erb D. K., Martin C. L., 2021, *AJ*, **161**, 212
- Reddy N. A., et al., 2015, *ApJ*, **806**, 259
- Reddy N. A., Topping M. W., Sanders R. L., Shapley A. E., Brammer G., 2023, *ApJ*, **952**, 167
- Rees M. J., Ostriker J. P., 1977, *MNRAS*, **179**, 541
- Reichardt Chu B., et al., 2022, *MNRAS*, **511**, 5782
- Reichardt Chu B., et al., 2025, *MNRAS*, **536**, 1799
- Revalski M., et al., 2021, *ApJ*, **910**, 139
- Rieke M. J., et al., 2023, *PASP*, **135**, 028001
- Riffel R. A., 2010, *Ap&SS*, **327**, 239
- Rigby J., et al., 2023, *PASP*, **135**, 048001
- Rizzo F., Vegetti S., Fraternali F., Stacey H. R., Powell D., 2021, *MNRAS*, **507**, 3952
- Rizzo F., et al., 2023, *A&A*, **679**, A129
- Roberts-Borsani G. W., Saintonge A., Masters K. L., Stark D. V., 2020, *MNRAS*, **493**, 3081
- Rowland L. E., et al., 2024, *MNRAS*,
- Roy N., et al., 2024, *ApJ*, **970**, 69
- Rubin K. H. R., Prochaska J. X., Koo D. C., Phillips A. C., 2012, *ApJ*, **747**, L26
- Rubin K. H. R., Prochaska J. X., Koo D. C., Phillips A. C., Martin C. L., Winstrom L. O., 2014, *ApJ*, **794**, 156
- Runco J. N., et al., 2021, *MNRAS*, **502**, 2600
- Rupke D. S., Veilleux S., Sanders D. B., 2005, *ApJ*, **632**, 751
- Ruschel-Dutra D., et al., 2021, *MNRAS*, **507**, 74
- Sánchez Almeida J., Elmegreen B. G., Muñoz-Tuñón C., Elmegreen D. M., 2014a, *A&ARv*, **22**, 71
- Sánchez Almeida J., Morales-Luis A. B., Muñoz-Tuñón C., Elmegreen D. M., Elmegreen B. G., Méndez-Abreu J., 2014b, *ApJ*, **783**, 45
- Sanders R. L., et al., 2016, *ApJ*, **816**, 23
- Sanders R. L., et al., 2021, *ApJ*, **914**, 19
- Sanders R. L., Shapley A. E., Topping M. W., Reddy N. A., Brammer G. B., 2023, *ApJ*, **955**, 54
- Sanders R. L., Shapley A. E., Topping M. W., Reddy N. A., Brammer G. B., 2024, *ApJ*, **962**, 24
- Saxena A., et al., 2024, *A&A*, **684**, A84
- Scarlata C., Hayes M., Panagia N., Mehta V., Haardt F., Bagley M., 2024, *arXiv e-prints*, p. [arXiv:2404.09015](https://arxiv.org/abs/2404.09015)
- Schaerer D., Marques-Chaves R., Barrufet L., Oesch P., Izotov Y. I., Naidu R., Guseva N. G., Brammer G., 2022, *A&A*, **665**, L4
- Scoville N., et al., 2017, *ApJ*, **837**, 150
- Shapley A. E., Reddy N. A., Sanders R. L., Topping M. W., Brammer G. B., 2023, *ApJ*, **950**, L1
- Speagle J. S., Steinhardt C. L., Capak P. L., Silverman J. D., 2014, *ApJS*, **214**, 15
- Spilker J. S., et al., 2020, *ApJ*, **905**, 85
- Stanton T. M., et al., 2024, *MNRAS*, **532**, 3102
- Steidel C. C., Erb D. K., Shapley A. E., Pettini M., Reddy N., Bogosavljević M., Rudie G. C., Rakic O., 2010, *ApJ*, **717**, 289
- Steidel C. C., Strom A. L., Pettini M., Rudie G. C., Reddy N. A., Trainor R. F., 2016, *ApJ*, **826**, 159
- Storey P. J., Hummer D. G., 1995, *MNRAS*, **272**, 41
- Strom A. L., Steidel C. C., Rudie G. C., Trainor R. F., Pettini M., Reddy N. A., 2017, *ApJ*, **836**, 164
- Strom A. L., Steidel C. C., Rudie G. C., Trainor R. F., Pettini M., 2018, *ApJ*, **868**, 117
- Sugahara Y., Ouchi M., Harikane Y., Bouché N., Mitchell P. D., Blaizot J., 2019, *ApJ*, **886**, 29
- Swinbank A. M., et al., 2019, *MNRAS*, **487**, 381
- Tacchella S., et al., 2022, *arXiv e-prints*, p. [arXiv:2208.03281](https://arxiv.org/abs/2208.03281)

- Tacconi L. J., Genzel R., Sternberg A., 2020, *ARA&A*, **58**, 157
- Tang M., Stark D. P., Chevillard J., Charlot S., 2019, *MNRAS*, **489**, 2572
- Tang M., et al., 2023, *MNRAS*, **526**, 1657
- Thompson T. A., Heckman T. M., 2024, *ARA&A*, **62**, 529
- Trump J. R., et al., 2023, *ApJ*, **945**, 35
- Trussler J. A. A., et al., 2023, *MNRAS*, **523**, 3423
- Tsukui T., Wisnioski E., Bland-Hawthorn J., Freeman K., 2024, *arXiv e-prints*, p. [arXiv:2409.15909](https://arxiv.org/abs/2409.15909)
- Tumlinson J., Peebles M. S., Werk J. K., 2017, *ARA&A*, **55**, 389
- Turner O. J., et al., 2017, *MNRAS*, **471**, 1280
- Übler H., et al., 2019, *ApJ*, **880**, 48
- Übler H., et al., 2023, *A&A*, **677**, A145
- Varidel M. R., et al., 2020, *MNRAS*, **495**, 2265
- Veilleux S., 1991, *ApJS*, **75**, 383
- Veilleux S., Cecil G., Bland-Hawthorn J., 2005, *ARA&A*, **43**, 769
- Veilleux S., Maiolino R., Bolatto A. D., Aalto S., 2020, *A&ARv*, **28**, 2
- Villar-Martín M., Humphrey A., Delgado R. G., Colina L., Arribas S., 2011, *MNRAS*, **418**, 2032
- Vogelsberger M., Genel S., Sijacki D., Torrey P., Springel V., Hernquist L., 2013, *MNRAS*, **436**, 3031
- Wang Y.-Y., Lei L., Yuan G.-W., Fan Y.-Z., 2023, *ApJ*, **954**, L48
- Wechsler R. H., Tinker J. L., 2018, *ARA&A*, **56**, 435
- Weiner B. J., et al., 2009, *ApJ*, **692**, 187
- Weldon A., et al., 2023, *MNRAS*, **523**, 5624
- Weldon A., et al., 2024, *MNRAS*, **531**, 4560
- White S. D. M., Frenk C. S., 1991, *ApJ*, **379**, 52
- Whitler L., Stark D. P., Endsley R., Leja J., Charlot S., Chevillard J., 2023, *MNRAS*, **519**, 5859
- Wisnioski E., et al., 2015, *ApJ*, **799**, 209
- Wuyts S., et al., 2016, *ApJ*, **831**, 149
- X. Xu X., et al., 2024, *arXiv e-prints*, p. [arXiv:2409.19776](https://arxiv.org/abs/2409.19776)
- Xu X., et al., 2022a, *ApJ*, **933**, 202
- Xu X., et al., 2022b, *ApJ*, **933**, 222
- Xu Y., Ouchi M., Nakajima K., Harikane Y., Isobe Y., Ono Y., Umeda H., Zhang Y., 2023, *arXiv e-prints*, p. [arXiv:2310.06614](https://arxiv.org/abs/2310.06614)
- Y. Xu Y., et al., 2024, *arXiv e-prints*, p. [arXiv:2404.16963](https://arxiv.org/abs/2404.16963)
- Yang H., Malhotra S., Rhoads J. E., Wang J., 2017, *ApJ*, **847**, 38
- Yu X., et al., 2019, *MNRAS*, **486**, 4463
- Zhang Y., Ouchi M., Nakajima K., Harikane Y., Isobe Y., Xu Y., Ono Y., Umeda H., 2024, *ApJ*, **970**, 19
- de Graaff A., et al., 2024, *A&A*, **684**, A87
- del Valle-Espinosa M. G., Sánchez-Janssen R., Amorín R., Fernández V., Sánchez Almeida J., García Lorenzo B., Papaderos P., 2023, *MNRAS*, **522**, 2089
- van de Voort F., Schaye J., Booth C. M., Haas M. R., Dalla Vecchia C., 2011, *MNRAS*, **414**, 2458
- van der Wel A., et al., 2022, *ApJ*, **936**, 9

APPENDIX A: DATA TABLES

In this appendix, we compile the main data and products used in this article. Specifically, Table A1 lists the physical and emission line properties of GO1871 galaxies; Table A2 summarizes the results from the morphological modeling and subsequent dynamical quantities; and Table A3 includes the gas-flow derived parameters for the gas flow candidates in the GO1871 sample.

This paper has been typeset from a $\text{\TeX}/\text{\LaTeX}$ file prepared by the author.

Table A1. Physical properties derived from SED fitting and emission line ratios for GO1871 galaxies.

MSAid	RA (deg.)	Dec (deg.)	z_{spec} (AB)	M_{UV} (M_{\odot})	$\log M_{\star}$ ($M_{\odot}\text{yr}^{-1}$)	SFR_{10} ($M_{\odot}\text{yr}^{-1}$)	SFR_{100}	$\log O_{32}$	$\log R_{23}$
1871 – 9	189.16626246	62.31651129	6.5691	–19.7	9.00 ± 1.17	$1.6^{+3.3}_{-1.6}$	$2.3^{+3.3}_{-1.6}$	–	–
1871 – 10	189.22199791	62.31576868	7.5990	–20.0	7.96 ± 0.39	$6.0^{+1.2}_{-1.6}$	$0.9^{+0.8}_{-0.2}$	≤ 1.04	≥ 0.63
1871 – 11	189.22436984	62.31137047	7.6100	–21.1	9.07 ± 0.31	$0.1^{+0.7}_{-0.1}$	$9.7^{+7.0}_{-2.5}$	≤ 1.60	≥ 1.07
1871 – 12	189.15797785	62.30239809	7.5020	–21.1	8.31 ± 0.09	$19.9^{+3.0}_{-2.1}$	$2.0^{+0.3}_{-0.2}$	0.73 ± 0.01	0.96 ± 0.05
1871 – 14	189.22515469	62.28628471	7.2049	–19.9	9.31 ± 0.17	$3.7^{+17.8}_{-1.2}$	$3.2^{+2.3}_{-1.6}$	0.95 ± 0.01	1.08 ± 0.08
1871 – 29	189.18882760	62.26991420	5.0191	–20.3	9.24 ± 0.22	$0.0^{+0.1}_{-0.0}$	$10.7^{+3.1}_{-3.0}$	0.64 ± 0.01	1.04 ± 0.04
1871 – 40	189.21508726	62.31794769	7.0948	–20.5	8.47 ± 0.53	$9.2^{+4.8}_{-3.1}$	$2.2^{+2.4}_{-0.9}$	≤ 0.64	≥ 0.69
1871 – 63	189.17219338	62.30563914	5.5872	–19.9	7.84 ± 0.34	$4.9^{+0.9}_{-0.9}$	$0.6^{+0.3}_{-0.1}$	1.54 ± 0.00	0.89 ± 0.01
1871 – 70	189.20956983	62.29928187	7.0302	–19.3	8.85 ± 0.41	$1.5^{+1.1}_{-1.1}$	$1.7^{+1.3}_{-0.9}$	≤ 0.68	≥ 0.56
1871 – 105	189.14873069	62.28092990	6.5669	–19.5	7.81 ± 0.79	$2.8^{+1.0}_{-1.2}$	$0.5^{+1.6}_{-0.2}$	–	–
1871 – 451	189.23835414	62.28442312	4.4615	–19.0	7.99 ± 0.59	$1.7^{+0.6}_{-1.0}$	$0.6^{+0.8}_{-0.3}$	0.31 ± 0.02	0.81 ± 0.07
1871 – 545	189.14071083	62.27725108	4.0416	–19.3	9.41 ± 0.41	$66.7^{+38.6}_{-39.7}$	$16.6^{+9.6}_{-5.9}$	-0.02 ± 0.01	0.86 ± 0.02
1871 – 912	189.18613720	62.27089253	6.7161	–21.8	9.69 ± 0.20	$3.8^{+9.8}_{-3.6}$	$27.1^{+14.8}_{-11.4}$	0.67 ± 0.01	1.06 ± 0.05
1871 – 918	189.20254167	62.27558333	6.9062	–20.6	8.78 ± 0.58	$6.5^{+5.7}_{-4.3}$	$3.9^{+3.6}_{-2.4}$	1.27 ± 0.04	0.62 ± 0.12
1871 – 969	189.15554992	62.28678755	6.5613	–19.0	7.80 ± 0.55	$1.5^{+0.7}_{-1.2}$	$0.5^{+0.7}_{-0.3}$	–	–
1871 – 1032	189.19565216	62.28247165	7.0889	–19.7	9.07 ± 0.24	$0.0^{+0.2}_{-0.0}$	$6.3^{+1.3}_{-1.7}$	≤ 0.69	≥ 1.24

Notes. Column 1: MSA object identifier. Column 2: source coordinates (RA and Dec). Column 3: spectroscopic redshift. Column 4: UV magnitude (AB). Column 5: stellar mass (in M_{\odot}) from SED fitting. Columns 6 and 7: SED-derived SFRs (in $M_{\odot}\text{yr}^{-1}$), averaged over 10Myr and 100Myr. Columns 8 and 9: O_{32} (ionization) and R_{23} (excitation) ratios.

Table A2. Morphological characterization and dynamical properties of GO1871 galaxies.

MSAid	NIRCam band	model	r_e (arcsec)	q	PA (deg.)	r_{phys} (pc)	Σ_{SFR} ($M_{\odot}\text{yr}^{-1}\text{kpc}^{-2}$)	σ_{res} (km s^{-1})	σ_{gas} (km s^{-1})	$\log M_{\text{dyn}}$ (M_{\odot})
1871 – 9	F182M	PSF	≤ 0.07	0.00	0	≤ 404	≥ 6.0	30.1	≤ 52.5	≤ 9.64
1871 – 10	F444W	Sérsic	0.14 ± 0.05	0.17	68	739 ± 262	2.3 ± 0.3	36.5	65.2 ± 5.3	9.54 ± 0.16
1871 – 11	F444W	Sérsic	0.17 ± 0.01	0.23	161	846 ± 37	0.3 ± 0.2	29.4	60.9 ± 12.9	9.77 ± 0.15
1871 – 12	F444W	Sérsic	0.07 ± 0.01	0.44	114	381 ± 39	20.3 ± 2.1	32.7	67.3 ± 2.8	9.41 ± 0.05
1871 – 14	F444W	PSF	≤ 0.07	0.00	0	≤ 383	≥ 8.2	31.8	≤ 60.5	≤ 9.72
1871 – 29	F444W	Sérsic	0.13 ± 0.01	0.60	95	839 ± 83	0.7 ± 0.1	38.5	72.0 ± 0.7	9.96 ± 0.04
1871 – 40	F182M	Sérsic	0.14 ± 0.01	0.38	177	740 ± 45	1.2 ± 0.3	31.6	60.6 ± 5.9	9.73 ± 0.07
1871 – 63	F444W	PSF	≤ 0.07	0.00	0	≤ 442	≥ 9.1	38.5	≤ 45.0	≤ 9.66
1871 – 70	F182M	Sérsic	0.12 ± 0.01	0.43	105	659 ± 52	1.7 ± 0.5	29.0	41.3 ± 8.0	9.42 ± 0.12
1871 – 105	F182M	Sérsic	0.07 ± 0.01	0.25	34	393 ± 41	4.8 ± 0.4	34.7	49.9 ± 1.4	9.34 ± 0.05
1871 – 451	F182M	Sérsic	0.08 ± 0.01	0.67	78	556 ± 66	0.8 ± 0.1	26.7	40.7 ± 2.5	9.37 ± 0.06
1871 – 545	F444W	Sérsic	0.12 ± 0.01	0.70	57	828 ± 88	1.2 ± 0.1	29.9	96.4 ± 1.4	10.11 ± 0.05
1871 – 912	F444W	Sérsic	0.18 ± 0.01	0.46	116	970 ± 59	1.0 ± 0.1	34.7	44.4 ± 1.9	9.68 ± 0.04
1871 – 918	F444W	PSF	≤ 0.07	0.00	0	≤ 393	≥ 5.7	29.4	≤ 62.1	≤ 9.73
1871 – 969	F210M	PSF	≤ 0.07	0.00	0	≤ 405	≥ 2.4	31.7	≤ 57.5	≤ 9.71
1871 – 1032	F182M	Sérsic	0.11 ± 0.01	0.42	83	600 ± 37	0.3 ± 0.3	36.1	37.3 ± 12.1	9.41 ± 0.16

Notes. Column 1: MSA object identifier. Column 2 and 3: NIRCam band and model used in the morphological fitting. Columns 4, 5, 6 and 7: best-fit effective radius (in arcsec), axis ratio, position angle (in deg.) and physical radius (in pc). Column 8: SFR surface density (in $M_{\odot}\text{yr}^{-1}\text{kpc}^{-2}$). Column 9: instrumental resolution from MSAFIT. Column 10: velocity dispersion of the ionized gas (in km s^{-1}) as given by the width of the [O III] $\lambda 5007$ lines, corrected by instrumental broadening. Column 11: inferred galaxy dynamical mass (in M_{\odot}).

Table A3. Gas flow parameters of GO1871 galaxies.

MSAid	F_B/F_N	σ_{narrow} (km s^{-1})	σ_{broad} (km s^{-1})	v_{flow} (km s^{-1})	\dot{M}_{flow} ($M_{\odot}\text{yr}^{-1}$)	η
1871 – 10	0.98 ± 0.32	49.08 ± 6.40	121.70 ± 29.95	(–) 179.90 ± 41.03	0.51 ± 0.16	0.09 ± 0.03
1871 – 12	0.84 ± 0.13	59.75 ± 3.83	160.20 ± 19.22	(+) 200.12 ± 34.00	3.90 ± 0.78	0.20 ± 0.04
1871 – 14	0.17 ± 0.05	61.48 ± 2.16	110.64 ± 56.12	(–) 182.47 ± 62.74	≤ 0.59	≤ 0.16
1871 – 40	0.81 ± 0.28	60.35 ± 5.61	259.15 ± 60.62	(+) 264.08 ± 66.79	0.40 ± 0.16	0.04 ± 0.02
1871 – 105	0.42 ± 0.10	57.32 ± 1.98	103.17 ± 8.73	(–) 149.68 ± 29.37	1.09 ± 0.31	0.39 ± 0.13

Notes. Column 1: MSA object identifier. Column 2: broad-to-narrow flux ratio. Columns 3 and 4: velocity dispersion of the narrow and broad components (in km s^{-1}). Column 5: maximum gas-flow velocity (in km s^{-1}). The (+) symbols denote red-shifted broad components respect to the narrow profiles, while sources marked with (–) are blue-shifted components. Column 6: mass flow rate (in $M_{\odot}\text{yr}^{-1}$). Column 7: estimated mass loading factor.